

ESTABLISHMENT OF A CLINICALLY RELEVANT LARGE ANIMAL MODEL TO ASSESS THE HEALING OF METAPHYSEAL BONE

F.I. Alagboso¹, M. Budak^{1,2}, U. Sommer¹, S. Ray¹, A. Kaiser¹, M. Kampschulte^{3,4}, A. Henss⁵, L. Dürselen⁶, C. Biehl^{1,2}, K.S. Lips¹, C. Heiss^{1,2}, U. Thormann^{1,2} and V. Alt^{7,*}

¹Experimental Trauma Surgery, Justus-Liebig-University Giessen, Giessen, Germany

²Department of Trauma, Hand and Reconstructive Surgery, University Hospital Giessen-Marburg GmbH, Giessen, Germany

³Laboratory of Experimental Radiology, Justus-Liebig-University Giessen, Giessen, Germany

⁴Department of Diagnostic and Interventional Radiology, University Hospital Giessen-Marburg GmbH, Giessen, Germany

⁵Institute for Physical Chemistry, Justus-Liebig-University Giessen, Giessen, Germany

⁶Institute of Orthopaedic Research and Biomechanics, Centre for Trauma Research, Ulm, Germany

⁷Department of Trauma Surgery, University Medical Centre, Regensburg, Germany

Abstract

Despite the high incidence of metaphyseal bone fractures in patients, the mechanisms underlying the healing processes are poorly understood due to the lack of suitable experimental animal models. Hence, the present study was conducted to establish and characterise a clinically relevant large-animal model for metaphyseal bone healing.

Six female adult Merino sheep underwent full wedge-shaped osteotomy at the distal left femur metaphysis. The osteotomy was stabilised internally with a customised anatomical locking titanium plate that allowed immediate post-operative full-weight bearing. Bone healing was evaluated at 12 weeks post-fracture relative to the untouched right femur.

Histological and quantitative micro-computed tomography results revealed an increased mineralised bone mass with a rich bone microarchitecture. New trabeculae healed by direct intramembranous ossification, without callus and cartilaginous tissue formation. Stiffness at the cortical and trabecular regions was comparable in both groups. Functional morphological analysis of the osteocyte lacunae revealed regularly arranged spherically shaped lacunae along with the canalicular network. Bone surface biochemical analysis using time-of-flight secondary-ion mass spectrometry showed high and homogeneously distributed levels of calcium and collagenous components. Ultrastructure imaging of the new trabeculae revealed a characteristic parallel arrangement of the collagen fibrils, evenly mineralised by the dense mineral substance. The specialised bone cells were also characterised by their unique structural features. Bone remodelling in the fractured femur was evident in the higher expression levels of prominent bone formation and resorption genes. In conclusion, the novel metaphyseal fracture model is beneficial for studying healing and treatment options for the enhancement of metaphyseal bone defects.

Keywords: Bone healing, metaphysis, adult sheep, locking plate, biomechanics, microstructure, ultrastructure.

***Address for correspondence:** Volker Alt, Department of Trauma Surgery, University Medical Centre, Regensburg, Germany.

Telephone number: +49 9419446805 Email: Volker.Alt@ukr.de

Copyright policy: This article is distributed in accordance with Creative Commons Attribution Licence (<http://creativecommons.org/licenses/by-sa/4.0/>).

Introduction

The healing of a diaphyseal fracture of the cortical bone area is mainly characterised by callus formation, with both intramembranous and endochondral ossification, where the amount of callus depends on the type and stability of the fracture fixation (Claes *et al.*, 1995; Claes *et al.*, 1997; Rabie *et al.*, 1996). In contrast, healing at the metaphyseal area occurs

mainly through a direct membranous bone formation in the trabecular region, with little or no callus formation (Claes *et al.*, 2011; Sandberg and Aspenberg, 2016; Uthoff and Rahn, 1981). There are many animal models for diaphyseal fracture healing, whereas only a very few *in vivo* models for metaphyseal bone healing, particularly in large animals (Alt *et al.*, 2013; Beil *et al.*, 2010; Claes *et al.*, 2009; Claes *et al.*, 2011; Fan *et al.*, 2008; Meyer *et al.*, 2001; Uthoff and Rahn, 1981).

Small animal models in comparison to large animal models are faced with several limitations, such as their small skeletal size, limited life expectancy, and different bone status as compared to the human situation (Komori, 2015; Martini *et al.*, 2001; Turner, 2002). Some of these shortcomings are addressable for bone healing studies by using larger animals, particularly sheep (Lill *et al.*, 2003; Martini *et al.*, 2001; Simpson and Murray, 2016; Turner, 2002; Zarrinkalam *et al.*, 2009). These studies have revealed major similarities between sheep and human bone in terms of size, microstructure, rate of bone healing, and mechanical properties, regardless of the variations in experimental conditions used in these studies, such as health status of the animal, species, age and skeletal site (Den Boer *et al.*, 1999; Turner *et al.*, 1995; Turner, 2002).

Although previous studies have confirmed the use of sheep as a large animal model for orthopaedic research, their use has not yet developed into a clinically relevant experimental animal model for metaphyseal bone healing. Most sheep fracture or bone defect models reported in the literature were carried out using defects created on skeletal sites other than the metaphyseal area of long bones (Aaron and Skerry, 1994; Christou *et al.*, 2014; Den Boer *et al.*, 1999). To the best of the authors' knowledge, only three studies are available on metaphyseal bone healing using sheep models. Malhotra *et al.* (2014) have compared the healing rate of different drill-hole defect sizes (8, 11 and 14 mm) created in the proximal tibia and distal femoral epiphysis of young and adult sheep. In the other two studies, the healing process of a 3 mm partial osteotomy, created in the trochlear groove of the distal femur in skeletally matured sheep (Claes *et al.*, 2009) and osteoporotic sheep (Bindl *et al.*, 2013), was studied. Despite having interesting experimental outcomes, the models mentioned are somewhat limited by the lack of full discontinuity of the bone at the fracture site and the absence of a clinically relevant fixation technique owing to the simple nature of the fracture, which is often not the case with clinical fractures. Based on current literature review, a complete discontinuity of bone at the metaphysis and proper internal fixation are among the main criteria required for an animal model to be considered clinically relevant for a metaphyseal bone healing study (Cheung *et al.*, 2016; Wong *et al.*, 2018).

The present study aimed to establish and characterise the healing outcome of a metaphyseal fracture model in the distal femur of a skeletally-mature sheep at 12 weeks post-fracture. This new model employed full discontinuity of bone at the metaphysis, where the fracture was internally stabilised with an anatomical locking titanium plate as commonly used in clinical practice. By employing both basic and specialised methods, including micro-computed tomography (μ CT), histology, biomechanics, quantitative PCR, time-of-flight secondary-ion mass spectrometry (ToF-SIMS) and

transmission electron microscopy (TEM), the healing outcome of the operated left femur was compared to the unoperated contralateral femur. ToF-SIMS is a very sensitive surface analytical technique that is used in the field of life science for evaluating the molecular and elemental components of biological tissues (Fletcher and Vickerman, 2010; Henss *et al.*, 2013). Thus, by employing ToF-SIMS, the level of bone matrix mineralisation at the fractured area were determined by differentiating the organic from the inorganic tissue components. TEM analysis enabled high-resolution imaging of the ultrastructural components of the new trabeculae, namely bone mineral material, collagenous fibrils and specialised bone cells (osteoblasts, osteoclasts and osteocytes).

Materials and Methods

Study design and ethics statement

The local animal care committee approved the study according to the German animal protection laws of the District Government of Darmstadt under the reference number V 54-19 c 20/15 - FU/1061. All the animals were handled in conformity with the guidelines for care and use of laboratory animals of the National Institutes of Health, Bethesda, MD, USA.

Six 6-7 years old female Merino land sheep, with an average weight of 99 kg, were used. Animals were fed with standard sheep diet (S6189-S010; Sondermischung Schaf, 4-mm pellet; ssniff-Spezialdiäten GmbH, Soest, Germany) and allowed free movement. 2 weeks after acclimatisation, the femoral osteotomy was performed. Thereafter, healing was allowed for 12 weeks, followed by euthanasia, sample harvesting and analysis using different methods.

Osteotomy at the distal femur metaphysis

A complete wedge-shaped osteotomy was created in the distal metaphyseal area of the left femur under sterile conditions and under general anaesthesia performed through intravenous administration of 2 mg/kg propofol (20 mg/mL propofol; Fresenius Kabi, Bad Homburg, Germany) and 2 mg/kg fentanyl (50 mg/mL Fentanyl-Hamel; Hameln Pharmaceuticals GmbH, Hameln, Germany). After draping the lateral region of the left thigh, incisions were made to expose the lateral femur from the lateral condyle area to the midshaft area between the *vastus lateralis* muscle and the lateral head of the femoral biceps muscle. For stable fixation of the distal femur, a custom-made angular stable 11-hole titanium plate (aap Implantate AG, Berlin, Germany) was inserted into the lateral side of the distal femur (Fig. 1a,b). Care was taken to fix the locking plate to the distal femur just proximal to the joint line of the knee joint and a non-locking screw was used to fix the plate onto the lateral cortex through the oval hole. Six 50 mm long locking screws (aap Implantate AG) were fixed into the distal part of the plate with penetration from the

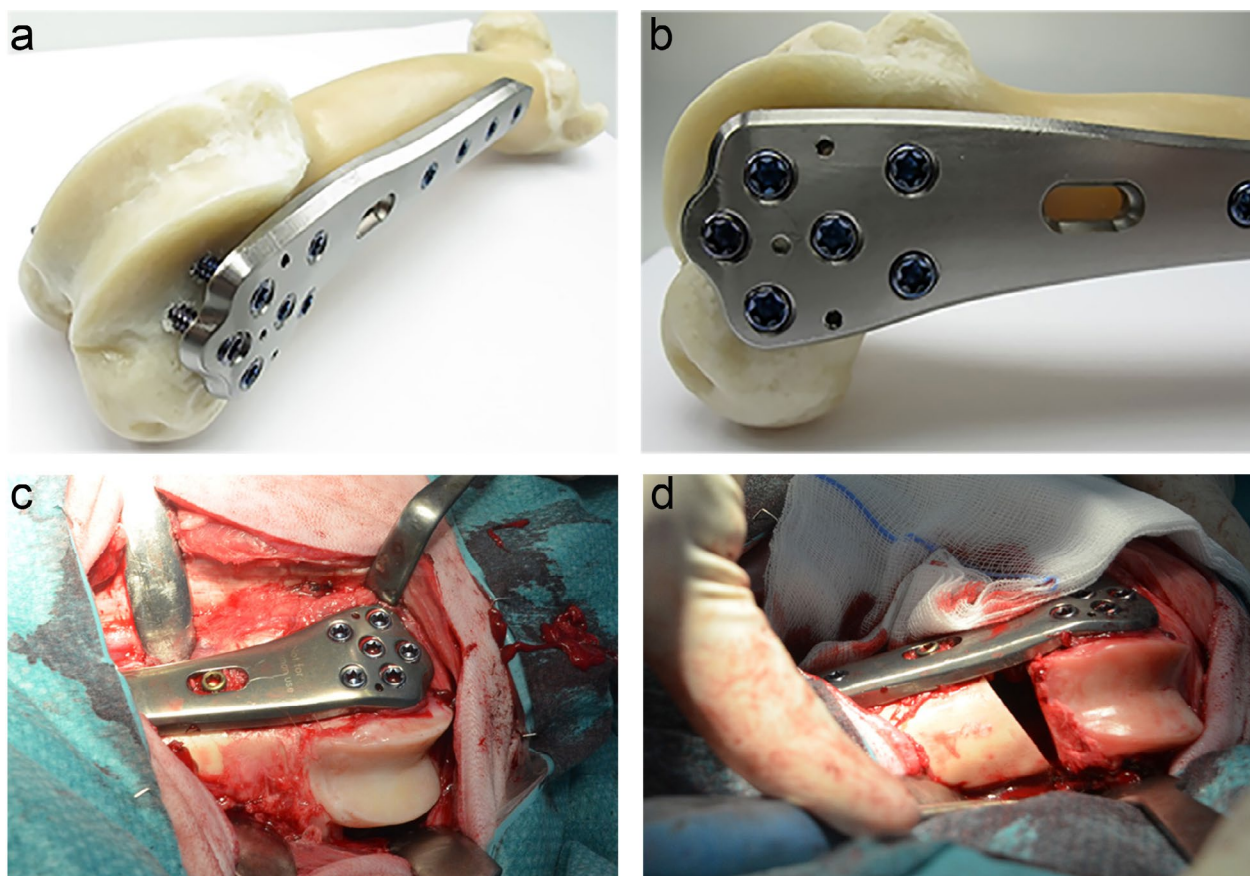


Fig. 1. Internal fixation of the custom-made locking plate and full osteotomy on the sheep distal femur metaphysis. (a) Overview image of the customised titanium locking plate for fixation of the distal metaphyseal area of the femur. (b) The condylar part of the plate allows for stable fixation of the distal femur with six 50 mm-long locking screws. (c) Intraoperative image after fixation of the locking plate to the lateral part of the left femur with stable fixation of the locking screws into the condylar area before osteotomy. (d) Intraoperative appearance after the creation of the wedge-shaped osteotomy with a full discontinuity at the femur distal metaphyseal area.

medial cortex, without violation of the cartilage or other intraarticular structures (Fig. 1c). The remaining locking screws were fixed into the diaphyseal region.

The patella was gently dislocated with the aid of blunt Hohmann retractors that exposed the ventral aspect of the distal femur. A line just proximal and parallel to the articular cartilage was marked. At the lateral aspect of the distal femur, the line was extended 10 mm proximally and connected to the medial origin of the line resulting in triangular/wedge-shaped guidelines for subsequent sawing. The osteotomy was carried out using a motorised oscillating saw. Afterwards, the created defect (Fig. 1d) was rinsed with sterile water and multiple-layered wound layer closure was performed. Resorbable stitches were used for skin closure. A spray silver dressing was applied to prevent infection. The stable angular fixation of the fracture permitted the immediate post-operative full-weight bearing. A short video clip showing the surgical procedure can be viewed (Supplementary video file).

Post-operative follow-up

Animals were kept separate for 1 week to ensure wound healing and for the rest of the observation

time in a flock on a nearby meadow, fed with standard diet and water *ad libitum*. General health status and wound healing were checked daily during the first 2 post-operative weeks by a veterinarian. This included administration of relevant analgesics, observation of weight bearing and return to daily activities. Thereafter, animals were monitored weekly until the end of the observation period. Post-operative X-ray of the femur on day 1 was performed without additional anaesthesia to ascertain if the metal implant was correctly placed and to exclude any additional peri-implant fractures of the femur.

Euthanasia and sample harvesting

All animals were euthanised at 12 weeks post-surgery by intravenous administration of 50 mg/kg pentobarbital (Anestestal; Pfizer) under general anaesthesia, as described above. After euthanasia, both left and right femora were harvested. Femora were carefully cleaned of any unwanted soft tissue in contact with the cortical bone surface and plates were carefully removed from the femora. All harvested femora remained stable after plate removal and no plate breakage was recorded. The distal ends of the operated left and unoperated right femora of the six

sheep were harvested and sectioned into thin coronal bone slices using a diamond saw (Trennband 0.2 mm; Patho-service, Oststeinbek, Germany) under constant cooling and, subsequently, assigned to various analytical methods. For biomechanical analysis, coronal bone slices of about 4.5 mm in thickness were immediately frozen without processing to avoid any alteration in bone quality. About 3 mm-thick coronal bone slices were allocated for gene expression and TEM analysis. Samples for gene expression analysis were immediately placed in RNAlater™ (1204027, Ambion) and stored at -80°C until further processing. 4.5 mm-thick coronal bone slices were allocated for both μCT analysis and histological staining, since μCT involved no specimen destruction. Bone specimens were immediately fixed in 4 % phosphate-buffered paraformaldehyde (Carl Roth) and stored at 4°C until further processing.

Sample processing

Coronal bone slices for histological analysis were embedded in Technovit® 9100 NEU, according to the manufacturer's protocol (Heraeus Kulzer, Hanau, Germany). Subsequently, samples were scanned for μCT measurements, followed by sample sectioning and staining. Newly formed trabeculae harvested within the fractured area were used for TEM analysis after prior embedding in Epon 812 type resin (Serva, Heidelberg, Germany), as briefly described below. Samples were cut into smaller pieces (1-2 mm thick) and fixed overnight at 4°C in yellow fix buffer and glutaraldehyde solution (Carl Roth). Afterwards, they were washed 9 times at 4°C in 0.1 M cacodylate buffer (Carl Roth) under vigorous shaking and, then, post-fixed in 1 % osmium tetroxide (Carl Roth) for 2 h at room temperature, followed by 6 rounds of washing in 0.1 M cacodylate buffer. Subsequently, samples were dehydrated through an ascending ethanol gradient, followed by xylene. Next, they were incubated for 72 h in 5 different infiltration solutions containing xylene and Epon 812 type mixtures in the following proportions:

1. 10 mL xylene + 5 mL Epon 812
2. 5 mL xylene + 5 mL Epon 812
3. 5 mL xylene + 10 mL Epon 812
4. 15 mL Epon 812
5. 15 mL Epon 812.

Finally, samples were embedded in Epon 812 type epoxy resin mixture, composed of 47.5 mL glycidyl ether resin (21045; Serva, Heidelberg, Germany), 20 mL of 2-dodecenylsuccinic acid anhydride (20755; Serva), 31 mL of methyl nadic-anhydride (29452; Serva) and 1.5 mL of 1.5 % 2,4,6-Tris (dimethylaminomethyl) phenol (20755; Serva) and polymerised for about 24 h at 60°C .

μCT scanning

Technovit-embedded coronal bone slices were scanned using a Bruker μCT (SkyScan 1173) at an X-ray energy of 130 kV and 60 μA for assessment of bone microstructure, as described by Boussein *et*

al. (2010). Samples were positioned on a computer-controlled rotation stage and scanned at 240° around the vertical axis in rotation steps of 0.25° with a noise reduction and a frame averaging of 4-fold. A 0.25 mm brass filter was used for beam filtration to reduce beam hardening. A pair of hydroxyapatite (HA)-phantoms with a diameter of 32 mm and mineral densities of 250-750 mg HA were scanned at each scan for system calibration of linear attenuation coefficient to the density of HA. Image reconstructions were carried out using the NRecon-Software (Bruker), resulting in an 8-bit grayscale image. A Gaussian filter (kernel = 1) was employed for image reconstruction with a moderate smoothing.

μCT image post-processing and data acquisition

Qualitative assessment of left femora bone specimen μCT images was performed by two independent investigators to determine the extent of bony bridging at both the cortical and trabecular regions of the fractured area. Examination was conducted with the Skyscan Dataviewer software (Bruker microCT, Kontich, Belgium) for three-dimensional (3D) image analysis. Before assessment, 3D images of bone slices were orientated in a similar direction. Then, the fractured area was divided into the following three parts: medial cortex, defect centre and lateral cortex. Healing at these regions was graded using the radiographic grading scale shown in Table 1, which was adapted from previous studies (Den Boer *et al.*, 1999; Malhotra *et al.*, 2014). Images were reviewed in transverse, coronal and sagittal planes to ensure a thorough and precise assessment. Sum of the grades was used to determine the healing status of each specimen.

For quantitative analysis, a direct 3D morphometry of the newly formed trabeculae of the operated left femur was analysed and compared to the unoperated right femur. Creation of region of interest (ROI), segmentation and quantitative morphometry were performed using the CTAn Software (Version 1.18.4, Bruker). A triangular/wedge-shaped ROI was

Table 1. Radiographic image grading scale.

0	No healing: no visible bone bridging within the fractured region.
1	Partial cortical and trabecular healing: minor bone bridging with gaps; defect visible, with lower radiographic density than adjacent bone outside the fractured region.
2	Advance cortical and trabecular healing: bone bridging evident with minimal gaps; defect visible, with radiographic density fairly similar to that of adjacent bone outside the fractured region.
3	Complete cortical and trabecular healing: bone bridging with no gaps; defect hardly visible, with radiographic density equivalent to adjacent bone outside the fractured region.

manually contoured within the fractured area of the operated left femur and at a comparable region in the unoperated right femur. Cortical bone region was excluded from the ROI. Wedge height at the lateral and medial sides of each bone sample was about 10.5 mm and 0.5 mm, respectively. Contoured wedge was interpolated into a defined specimen volume. For trabecular bone morphometry, a global threshold of 30 % of the maximum grey values corresponding to a mineral density of 400 mg HA/cm³ was defined. The analysis approach was adapted from previous reports (Morgan *et al.*, 2009; Nyman *et al.*, 2009).

Biomechanical analysis

Stiffness of the trabecular and cortical regions within and adjacent to the fractured area was determined using an indentation test. To enable comparison, similar points were also measured from the matching unoperated right femur. Non-processed fresh coronal bone sections with a thickness of about 4.5 mm were used for analysis. Samples were marked at nine points with a special water insoluble pen (Fig. 2). Points 2, 5, 7, 8 and 9 were within the fracture area, 1 and 3

were around the cortical region while 4 and 6 were located within the inner part of the bone adjacent to the fracture area. Thereafter, the indentation test was performed on the marked points using a standard material test machine (Z10, Zwick Roell, Ulm, Germany). The machine was fitted with a force sensor (500 N maximum load, KAF-Tw, A.S.T., Dresden, Germany) and the deformation was measured with a laser distance sensor (IL-D220-20, Mikro-Epsilon, Ortenburg, Germany). Samples were placed on an even surface and kept moist throughout the test using 0.9 % sodium chloride solution. After applying a preload of 5 N with a stamp of 2.6 mm in diameter, the indentation test was conducted at a constant deformation rate of 1 mm/min. Measurement was automatically terminated if either the sample failed to withstand the applied force or a compressive force of 120 N was reached. Stiffness (N/mm) was calculated from the linear part of the force-deformation curve. This occurred at an indentation depth of maximally 10 % of the sample height for trabecular bone and around 2 % of the sample height for cortical bone.

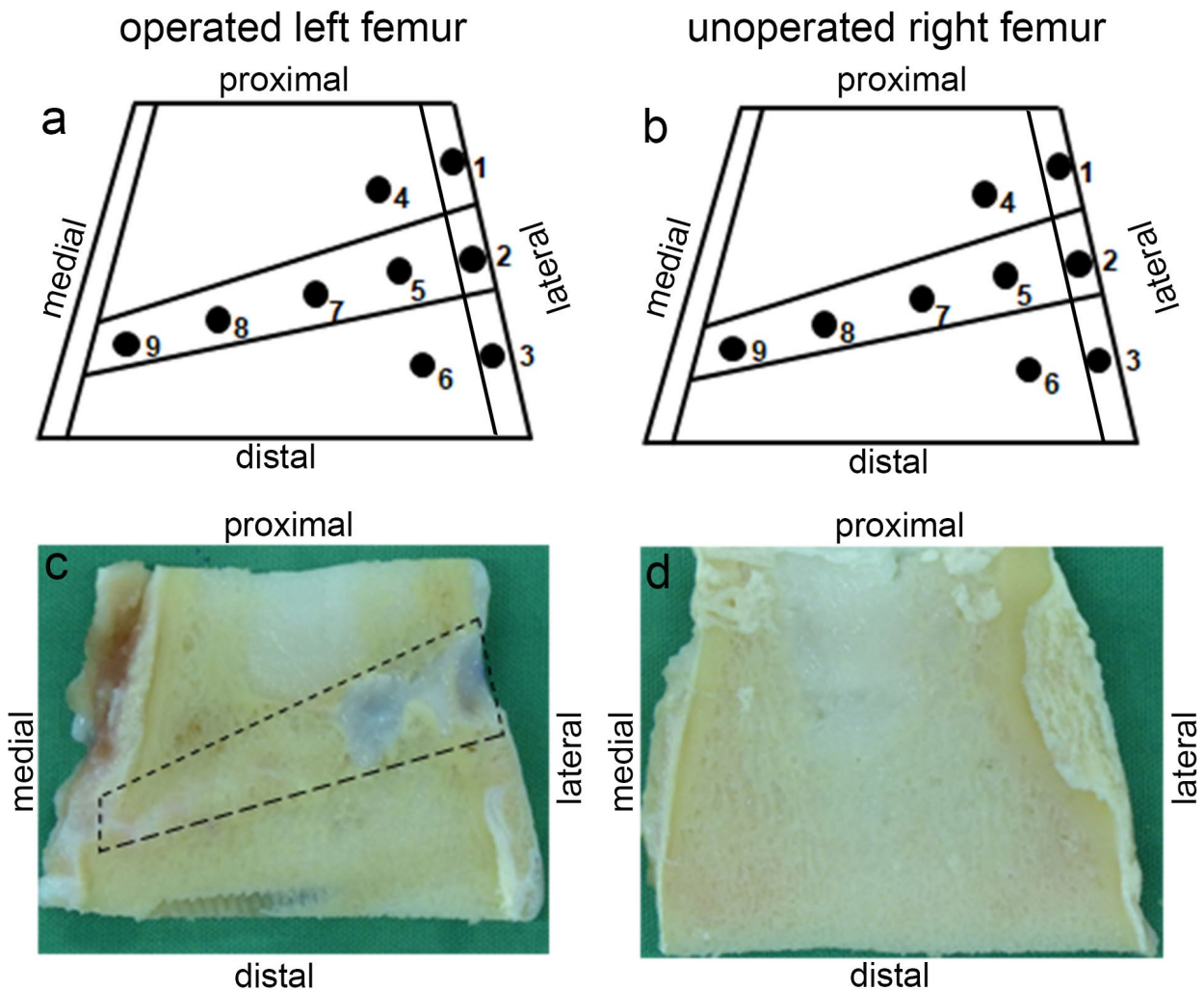


Fig. 2. Localisation of indentation points. Schematic representation of the measurement locations on the bone slices of the (a) operated left femur and (b) unoperated right femur. Photographs of coronal bone slices of the (c) operated left femur and (d) unoperated right distal femur. The dashed-wedge-shape outline shows the fractured area.

Histological analysis

A part of each of the Technovit-embedded samples was ground and polished to about 70 μm in thickness using a cutting-grinding machine (Exakt-300, EXAKT Advanced Technologies, Norderstedt, Germany); the remaining part was trimmed and sectioned into 5 μm -thick sections using the Kawamoto's film [Cryofilm type 2C (9), Section-Lab Co. Ltd., Hiroshima, Japan] on a microtome (RM2155, Leica) equipped with a hard-metal knife (400215, Leica). The undecalcified ground sections were stained with Masson-Goldner trichrome to investigate the microstructural features of the newly formed cortical and trabecular bone within the fractured area, as described below. Briefly, samples were deplastified in 2-methoxyethyl-acetate-1 (Merck) and, subsequently, rehydrated in a graded ethanol series. Samples were stained with Weigert's iron haematoxylin A + B (Carl Roth) and, then, in Masson solution prepared from Ponceau-fuchsin S-azophloxin compounds (Chroma, Münster, Germany). Afterwards, the samples were rinsed in 1 % acetic acid (Merck) and immersed in tungstophosphoric acid orange G solution (Merck and Chroma). Finally, samples were stained with 0.2 % light green (Fluka), rinsed in 1 % acetic acid and dehydrated very rapidly in 100 % ethanol followed by clearing in xylene (Carl Roth).

Undecalcified bone sections were stained with von Kossa-van Gieson to differentiate the mineralised bone area from the osteoid area and to quantify the newly mineralised bone within the fractured area, as described briefly below. Samples were deplastified in 2-methoxyethyl-acetate and, then, rehydrated in a decreasing ethanol series. Thereafter, samples were stained with von Kossa by incubation for 5 min in 3 % silver nitrate solution (131459, Applichem) and for about 2 min in 10 % sodium carbonate-formaldehyde solution. Subsequently, samples were fixed in 5 % sodium-thiosulphate solution (Merck) for 5 min and contrasted in 0.8 % methyl green solution (Carl Roth) for 8 min. Next, samples were stained with van Gieson by incubation in Weigert's iron haematoxylin for 6 min, washing under flowing tap water for 10 min and immersion in van Gieson solution (Chroma) for 5 min. Thereafter, samples were dehydrated very quickly in ethanol and cleared in xylene.

Undecalcified bone sections were stained with silver nitrate to visualise the morphology of the osteocyte-lacuna canaliculi network and quantify the osteocyte lacunae within the fractured area. Briefly, after sample deplastification and rehydration, bone sections were decalcified in a solution containing 3.4 % Tris (Carl Roth) and 10 % Titriplex III (Merck) for 3 d. Thereafter, samples were stained with a silver nitrate mixture for 90 min in a dark chamber and, then, incubated in 5 % sodium-thiosulphate solution for 10 min. Subsequently, samples were dehydrated through an ascending ethanol gradient and cleared in xylene.

Light microscopy

Images were acquired using a Leica microscopy system (Leica DM5500 photomicroscope equipped with a DFC7000 camera and operated by LASX software version 3.0).

ToF-SIMS analysis

To study the local distribution of calcium and collagen within the fractured area, undecalcified coronal ground sections were scanned using the ToF-SIMS 5-100 machine (IONTOF Company, Münster, Germany) equipped with a 25 keV Bi-cluster ion source for surface analysis. ToF-SIMS method has been previously described (Schueler, 2013). Briefly, a primary ion gun using Bi^{3+} as main ion species was operated in the high current bunched (hc-bu) mode with the highest mass resolution and a lateral resolution of about 10 μm . Ca^+ signal represented the mineralised area while signals collected from $\text{C}_4\text{H}_8\text{N}^+$, a proline fragment, which is one of the main components of collagen, was used to image the collagen distribution (Henss *et al.*, 2013). To obtain a good mass image of the bone slice, an entire stage scan with a density of 100 pixel/mm, a cycle time of 60 μs , 5 frames per patch and 3 scans were generated. Single images with sizes of $400 \times 400 \mu\text{m}^2$ were stitched together to obtain areas of several mm^2 . Data evaluation was performed with Surface Lab 6.7 software of IONTOF Company.

Ultramicrotomy

Epon-embedded samples were first cut into semi-thin 0.5 μm -thick sections. Sections were stained with toluidine and safranin O solution and, then, visualised using the light microscope to localise the ROI for further electron microscope investigation. Then, ultra-thin sections in the range of 60-80 nm thickness were cut from the localised region using an ultra-microtome (Reichert-Jung ultra-cut 701701, Leica microsystems, Wetzlar, Germany) equipped with a diamond knife (DU3525, Diatome, Nidau, Switzerland). Subsequently, sections were contrasted with 0.5 % uranyl acetate (Ultrastain 1, Laurylab, Brindas, France) for 30 min and 3 % lead citrate (Ultrastain 2, Leica) for 80 s using the Leica contrasting machine (Leica EM AC20) according to the manufacturer's protocol.

TEM

Images were acquired using a Zeiss TEM system (Zeiss EM912 OMEGA) equipped with a camera (TRS Sharp Eye 2k slow-scan CCD, Tröndle, Moorenweis, Moorenweis) and controlled by the Olympus iTEM software (Olympus, Tokyo, Japan).

Gene expression analysis

Fresh-frozen bone slices stored in RNAlater solution at -80°C were thawed at room temperature. Newly formed trabeculae within the fractured area of the operated femur were carefully selected. For

comparison, trabecular bone was also collected from the metaphyseal area of the unoperated contralateral side. Subsequently, about 50 mg were collected from each sample with the aid of forceps for RNA isolation using the Lipid Tissue Mini Kit (160021969, Qiagen) according to the manufacturer's protocol. Isolated RNA was quantified using the NanoDrop™ 1000 Spectrophotometer (NanoDrop Technologies, Wilmington, Delaware, USA). After DNase treatment to remove genomic DNA, 0.5 µg RNA from each sample were reverse transcribed to cDNA using the QuantiTect Reverse Transcription Kit (157036867, Qiagen), as described by the manufacturer.

Quantitative PCR analysis of major bone formation markers, namely bone morphogenetic protein-2 (*BMP2*), osteoprotegerin (*OPG*), alkaline phosphatase (*ALP*), osteocalcin (*BGLAP*), collagen type-1 alpha-1 (*COL1A1*) and collagen type-2 alpha-1 (*COL2A1*), and bone resorption markers, including receptor activator of NF-κB ligand (*RANKL*) and cathepsin-K (*CTSK*), was performed with the Quantifast SYBR Green PCR Mastermix kit (151050429, Qiagen) on the LightCycler® 2.0 instrument (software version 4.1, Roche). Beta-2 microglobulin (*B2M*) was used as reference gene. The thermal cycling program comprised of 1 denaturation cycle at 95 °C for 5 min followed by 40 cycles at 95 °C for 10 s and at 60 °C for 30 s. Specificity of the amplicon was verified with a melting curve analysis: temperature was gradually increased to 95 °C, followed by 15 s at 60 °C and subsequent return to 95 °C. The final cycle was a cooling step at 40 °C for 30 s. Each sample was treated in duplicate with necessary controls. Mean values were determined and normalised to the reference gene, *B2M*. Afterwards, relative expression of the target gene of the operated left femur was compared to that of the unoperated right femur using the $2^{-\Delta\Delta CT}$ method (Livak and Schmittgen, 2001). Forward and reverse sequence of all the primers and the amplicon length are reported in Table 2.

Statistical analysis

Data analysis and graphical presentations were carried out using GraphPad Prism 7.0 (GraphPad Software Inc.) and SPSS (V.22.0, SPSS Inc.). All results are presented as means ± standard error of the mean. Mean values from the operated left femur

were compared with those of the unoperated right femur using the Wilcoxon matched-pairs signed rank test or paired Student's *t*-test. $p < 0.05$ was considered statistically significant.

Results

Clinical observations

All six animals tolerated the 10 mm osteotomy gap created at the distal metaphyseal area of the left femur. They returned to their normal activity and full load bearing around day 3 post-surgery. Post-operative X-ray of the femur revealed the fractured gap at the metaphyseal area of the distal femur with correct placement of the plate and locking screws that extended into the epiphysis for better stability of the fracture (Fig. 3a,b). All sheep survived throughout the observation period without any plate breakage, fracture or other relevant adverse events and could be euthanised according to the study protocol.

µCT analysis

Healing quality at the fractured area was determined by a macroscopic analysis of the reconstructed 3D µCT images of the bone slices. Qualitatively, images of all samples revealed a complete bridging of the fracture gap from the medial side up to two-thirds of the fractured area. Four out of six samples (Fig. 4a-d) achieved almost complete bridging of the entire fracture gap from the medial to the lateral cortex; the remaining two samples attained partial healing (Fig. 4e,f). Blind scoring of the healing degree by two independent investigators ranged between 4 and 8.5 from a total score of 9 (Fig. 5).

Direct 3D-quantitative morphometry of a defined ROI within the trabecular bone area of the operated femur and a corresponding region within the unoperated femur showed that bone volume (BV) and bone volume to total volume ratio (BV/TV) were comparable in both femora (Fig. 6a,b). Also, the number of trabeculae within the healed femora was comparable to the unoperated contralateral side (Fig. 6c). However, thickness and spacing of the trabeculae were significantly increased in the operated femora when compared to the unoperated side (Fig. 6d,e). The structural model index (SMI), a parameter for

Table 2. Forward and reverse primer sequence of the target genes.

Target gene	Forward sequence (5'-3')	Reverse sequence (5'-3')	Amplicon length (bp)
BGLAP	CAGCGAGGTGGTGAAGAGAC	GCTCATCACAGTCAGGGTTG	122
CTSK	GGGTCAATGTGGTTCCTGTT	GCAGCCATCATTCTCAGACA	133
COL1A1	CCAGTCACCTGCGTACAGAACG	GCCAGTGTCTCCTTTGGGTCC	246
ALP	TCAGCAGACCCTGAAAAATG	TTCTTAGCCACGTTGGTGTTG	60
BMP2	GAAAGGACACCCTCTCCACAG	GCAACGATCCAGTCATTCCAC	135
OPG	AAACAGCGACACAACCTCACG	TGTCCAATATGCCTCCTCACG	140
RANKL	CTGTGCAGAAGGAAATGCAAC	GCGTTAATCGTGAGATGGGC	139
COL2A1	ACCCAGAACCAACACAATCC	TCAGTGCAGAGTCCTAGAGTG	81
B2M	CCAGAAGATGGAAAGCCAAA	AGCGTGGGACAGAAGGTAGA	159

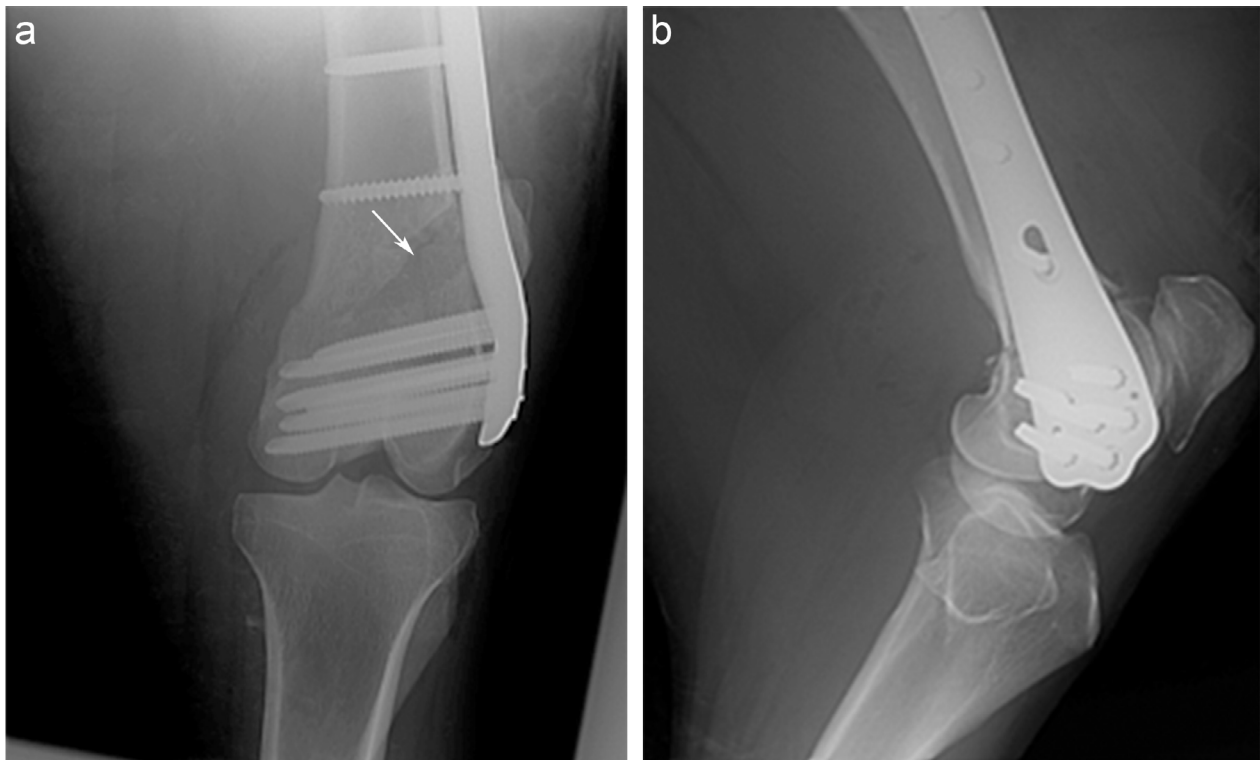


Fig. 3. Post-operative X-ray analysis of the operated femur. (a) Post-operative X-ray image on day 1 revealed the wedge-shaped metaphyseal fracture in the frontal plane on the anteroposterior view (arrow) fixed in place with locking plate and screws. (b) Lateral view showing proper alignment of the plate along the femur axis. The fracture is not visible on the lateral image due to the overlying plate.

estimating trabecular shape, was also significantly lower in the operated femora (Fig. 6f).

Bone biomechanical strength analysis

An indentation test on nine different points covering both the trabecular and cortical regions within the fractured region and sub-regions was performed on the bone slices to compare the stiffness of the operated left to the unoperated right femora. Quantitative assessment of the mechanical strength of the newly formed bone based on the degree of stiffness showed that the operated femora, both at the cortical and trabecular area, were not statistically different from the intact contralateral side (Fig. 7). Moreover, the stiffness at the cortical area of both operated and unoperated femora was about 2-fold more than in the trabecular area.

Qualitative histology

The overall microstructural appearance of the newly formed bone was determined by Masson-Goldner trichrome staining. An advanced bony bridging that correlated with radiological image was evident. Medially, there was both inter-cortical and trabecular bone bridging of the fractured area, as shown in the representative overview image of sheep 2 (Fig. 8a). The fractured area was almost completely bridged with new bone, as seen in the radiological image. Only a minor area within the trabeculae was bridged with soft connective tissue, mostly in the form of

dense collagenous fibres. The bridged cortical bone area revealed tightly-packed osteons of concentric lamellae, while the connective tissue area showed dense collagenous fibres (Fig. 8b,c). The newly formed trabecular bone revealed dense and well-structured trabeculae and marrow space enriched with adipose tissue, as the native bone lying outside the fractured area (Fig. 8d). Also, chondrocytes were absent in the fractured area. The new trabeculae formed through a direct membranous transformation into bone at the marrow cavity without any observable callus. However, a thin layer of periosteal callus was seen only at the medial end of the femoral cortex; whereas, at the lateral cortex, no external callus formation was visible. Furthermore, the level of the new bone matrix mineralisation was determined by von Kossa-van Gieson staining. The images revealed a large mineralised bone area (black staining) and a smaller osteoid area (pink staining) in the fractured area comparable to the native bone lying outside (Fig. 9a). The osteoid region surrounded the mineralised area and was majorly composed of dense collagenous fibres with numerous osteoblasts embedded within (Fig. 9b,c). Histomorphometric quantification of both areas revealed 40 % of a mineralised area and 20 % of an osteoid area.

The quality of the healing outcome in the fractured area was further characterised by quantifying osteocyte lacunae and morphological arrangement of the osteocyte-lacuna canaliculi network. Images of

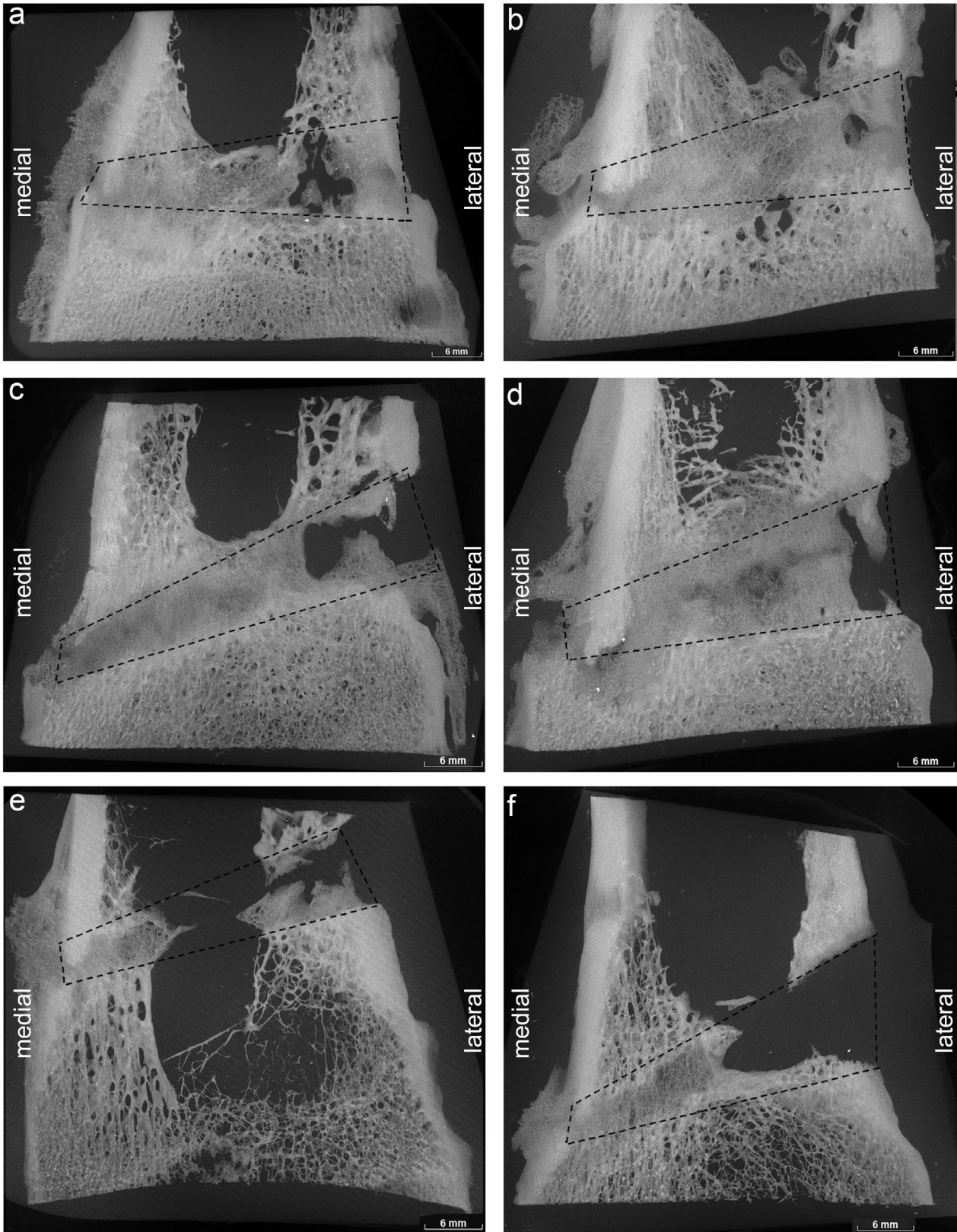


Fig. 4. μ CT image evaluation of the healing status of all six sheep at 12 weeks post-fracture. Four out of six sheep, namely sheep (a) 2, (b) 3, (c) 5 and (d) 6, showed almost complete bony bridging of the whole fractured area. Partial bony bridging of the fracture gap was seen in (e) sheep 1 and (f) 4. Wedge-shaped outline shows the fractured area.

decalcified bone sections stained with silver nitrate revealed mostly spherically shaped osteocytes lacunae organised in lamellae and interconnected through canaliculi, which resembled those of the unoperated contralateral side (Fig. 9d-f). The canalicular system was mostly arranged perpendicular to the longitudinal axis of the trabeculae. There was an increased number of osteocytes lacunae in the fractured area. However, the amount was significantly higher in the unoperated femora (Fig. 9g). Empty lacunae were mostly seen at the lateral cortex, where the least bone bridging occurred.

ToF-SIMS analysis

Local distribution pattern of calcium and collagen components of the newly formed bone within the fractured area was analysed by ToF-SIMS. Mass images of calcium and collagen, represented by Ca^+ and $C_4H_8N^+$ signals, respectively, as well as overlay images were generated (Fig. 10). Calcium mapping revealed a quite homogeneous calcium distribution, with increased calcium content in the cortical region. The colour scale encoded the signal intensity for each pixel, which meant the brighter the colour,

the more the detected signal. Collagen signal also showed a homogeneous distribution within the dense trabecular network. No obvious difference was seen in Ca^+ and collagen signal intensity between

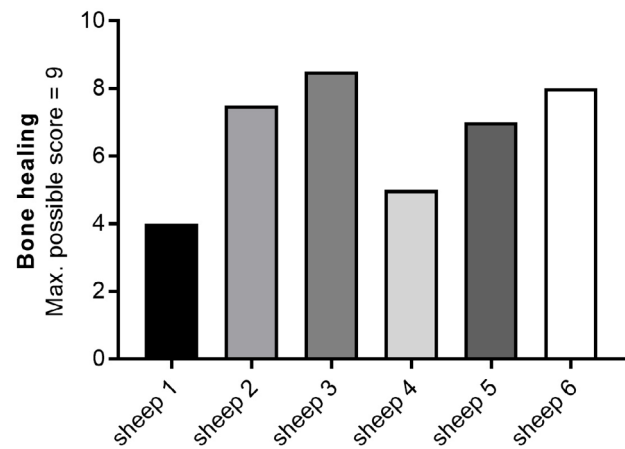


Fig. 5. Qualitative evaluation of the extent of bone healing. Healing score was determined from the macroscopic assessment of the fractured area from the medial cortex to the lateral side.

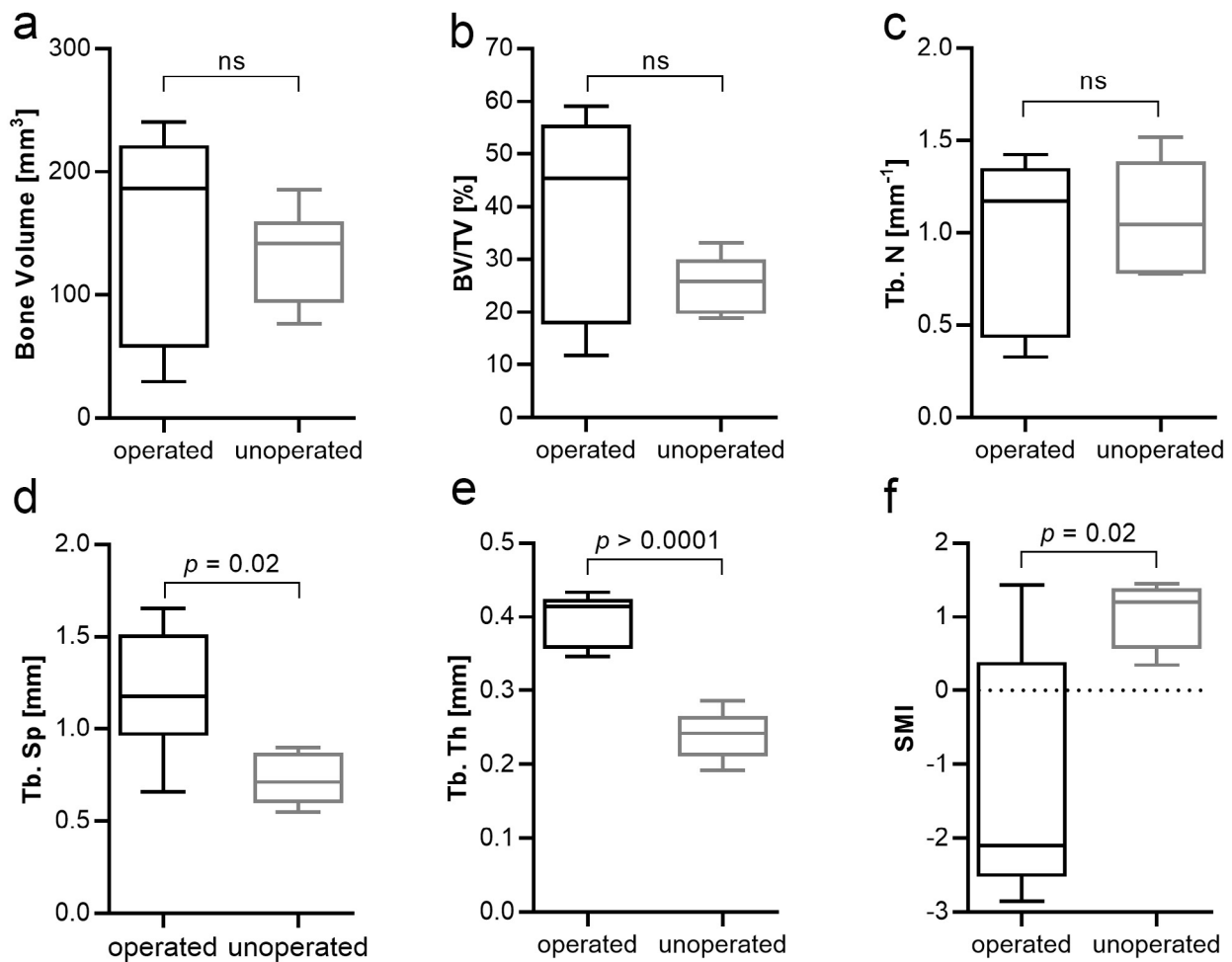


Fig. 6. Quantitative μ CT image analysis. A direct 3D quantitative morphometry of a defined ROI within the trabeculae of the operated left femur and the unoperated contralateral side showing positive structural changes of the new trabeculae as revealed by a higher (a) BV, (b) BV/TV and (c) comparable number of trabeculae (Tb.N). (d,e) Significantly higher trabecular spacing (Tb.Sp) and thickness (Tb.Th). (f) Negative SMI value. ns = not significant.

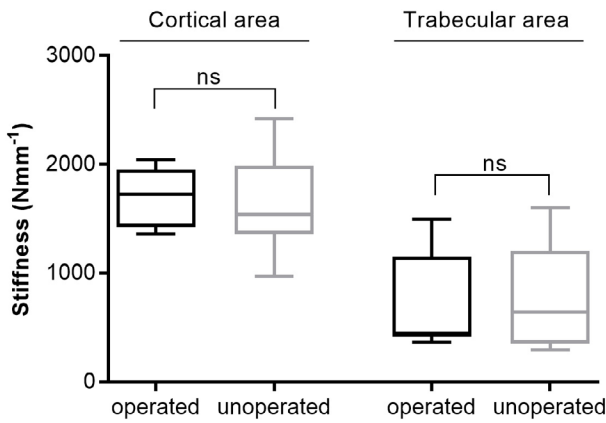


Fig. 7. Assessment of biomechanical competence of the newly formed bone. Bone stiffness at the cortical and trabecular areas of the operated and unoperated femora. Bone stiffness of the operated femur was not statistically different from the unoperated right femur. Stiffness was about two-fold higher in the cortical area of both groups.

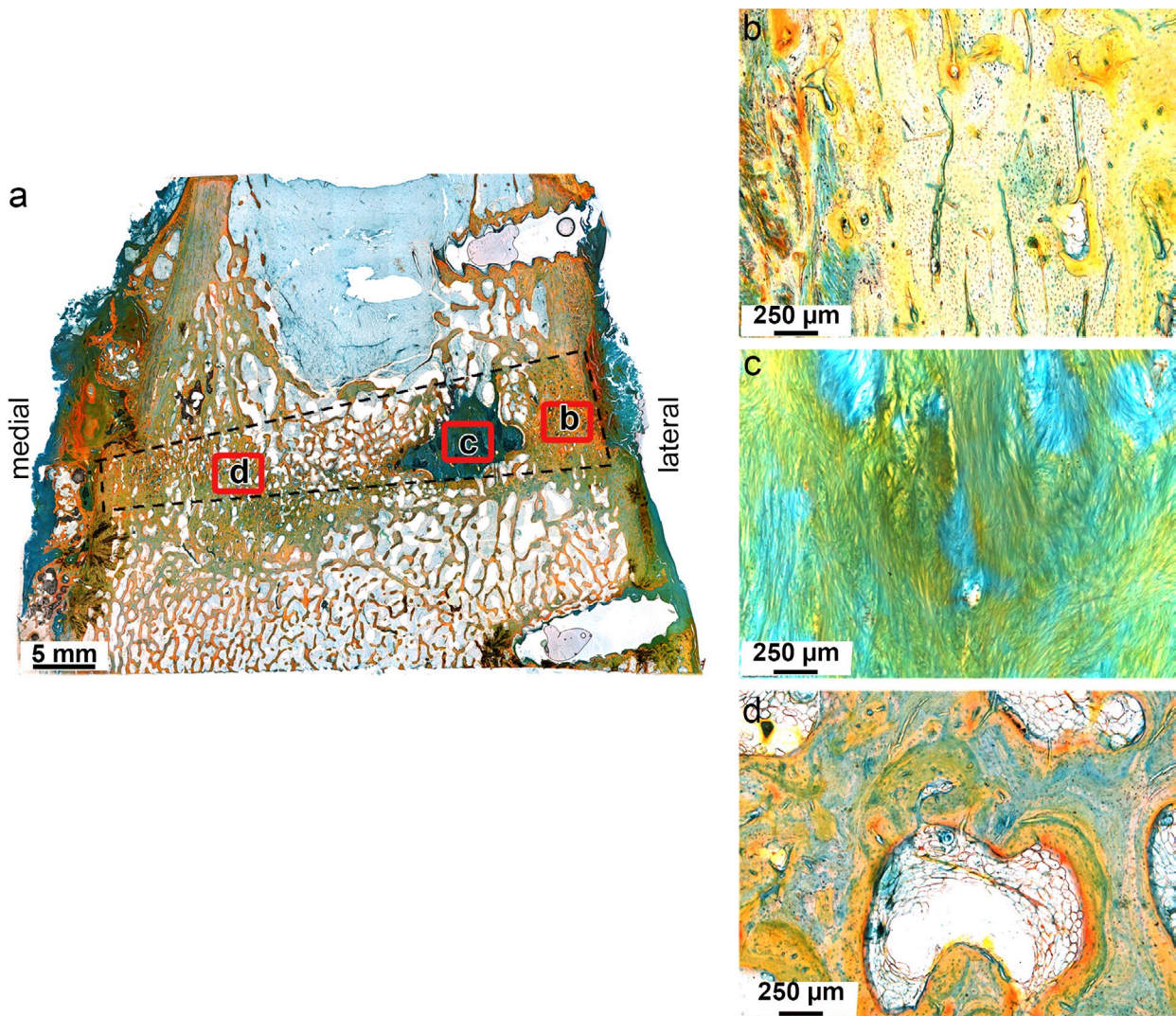


Fig. 8. Microstructural features of the newly formed cortical and trabecular bone in the fractured area. (a) Overview image of a coronal bone section of sheep number 2 stained with Masson-Goldner trichrome showing an advanced bony bridging at the fractured area. Gap was almost completely replaced with new bone with an appearance comparable to the native bone outside the fracture site. No callus formation was evident at the lateral cortex whereas a thin layer of periosteal callus was visible at the medial end. A minor area within the trabeculae was filled with soft connective tissue, marked as c. Detail images of (b) cortical bone area showing a compact mineralised cortex with the typical Haversian system, (c) connective tissue showing bundles of dense collagenous fibres and (d) trabecular bone area revealing dense and well-structured mineralised trabeculae with marrow cavity lying within. The mineralised bone area was stained greenish-orange and the unmineralised bone area was stained green.

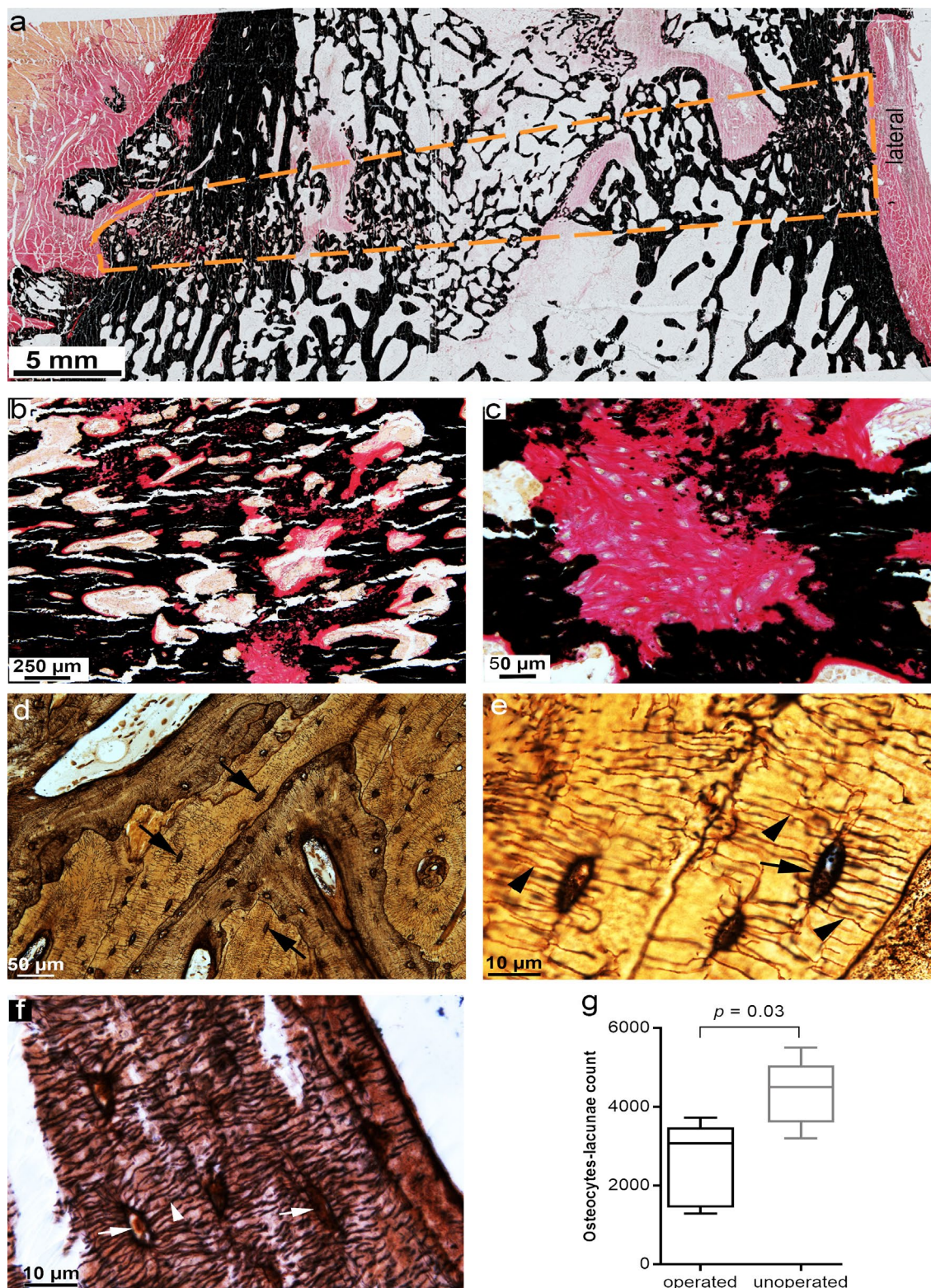


Fig. 9. Major bone matrix mineralisation and regularly arranged osteocytes lacunae with the canaliculi network as proof of new bone maturation. (a) Overview image of an undecalcified bone section of the operated femur stained with von Kossa-van Gieson showing the mineralised area in black and the osteoid area in pink within the fractured area, as represented with the dashed-line. (b) A close-up image of the fractured area revealed mainly mineralised bone area. (c) The minor osteoid area revealed collagenous fibres that surrounded and lined the surface of the mineralised bone with numerous osteoblasts cells embedded within. (d) Overview image of a decalcified silver nitrate stained bone section of the operated femur showing abundant spherically shaped osteocytes (arrows) regularly arranged within the trabecular lamellae. Close-up images of (e) operated and (f) unoperated femur revealed similar osteocyte-lacuna canaliculi network. The canaliculi networks were arranged perpendicular to the bone surface (arrowheads). (f) The number of the osteocyte lacunae was significantly higher in the unoperated femur.

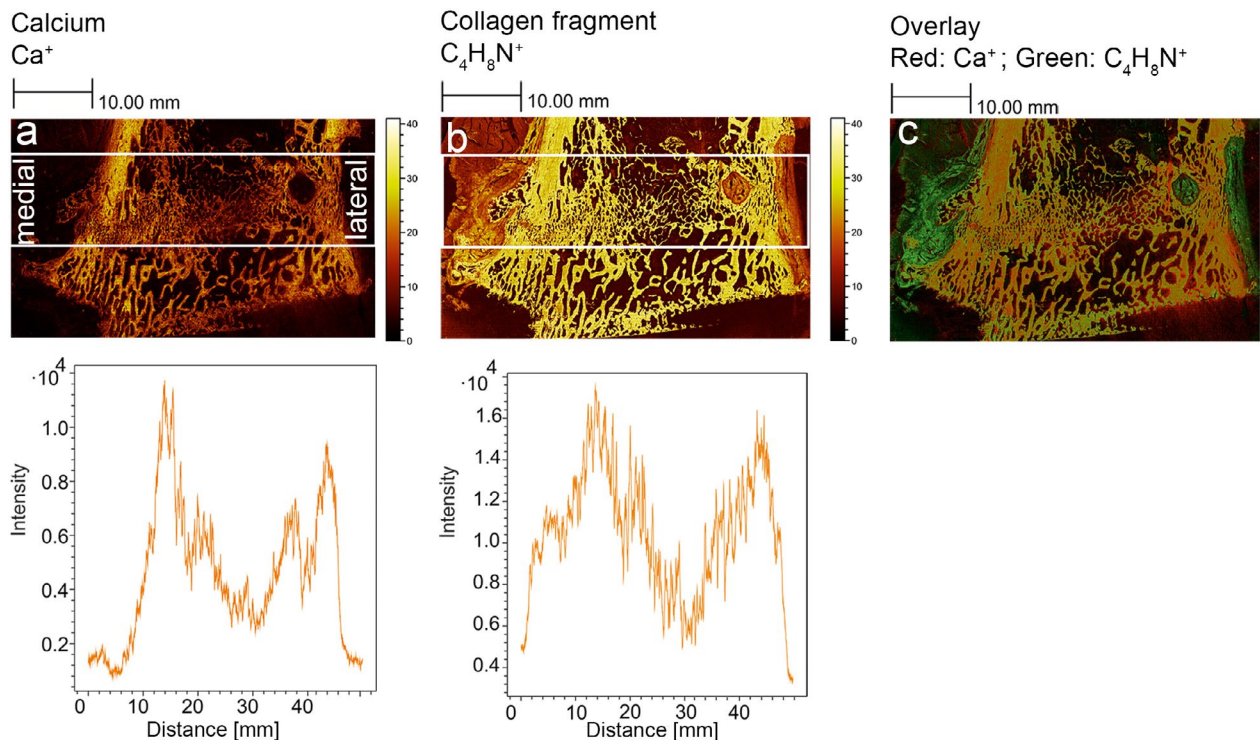


Fig. 10. Local distribution pattern of calcium and collagen in the fractured area. Mass images of (a) Ca^+ and (b) collagen fragment $\text{C}_4\text{H}_8\text{N}^+$ showed homogenous intensity distribution within and outside the fractured area. (c) An overlay image of calcium in red and collagen in green. Unmineralised collagen signal was detectable at the edge of the medial cortex. Line scans below the Ca^+ and $\text{C}_4\text{H}_8\text{N}^+$ mass images showed the signal intensity of calcium and collagen, respectively, within the fractured area, as marked with the white rectangle. Signal intensity generated in the y-axis was summed up and plotted against the distance in the x-axis.

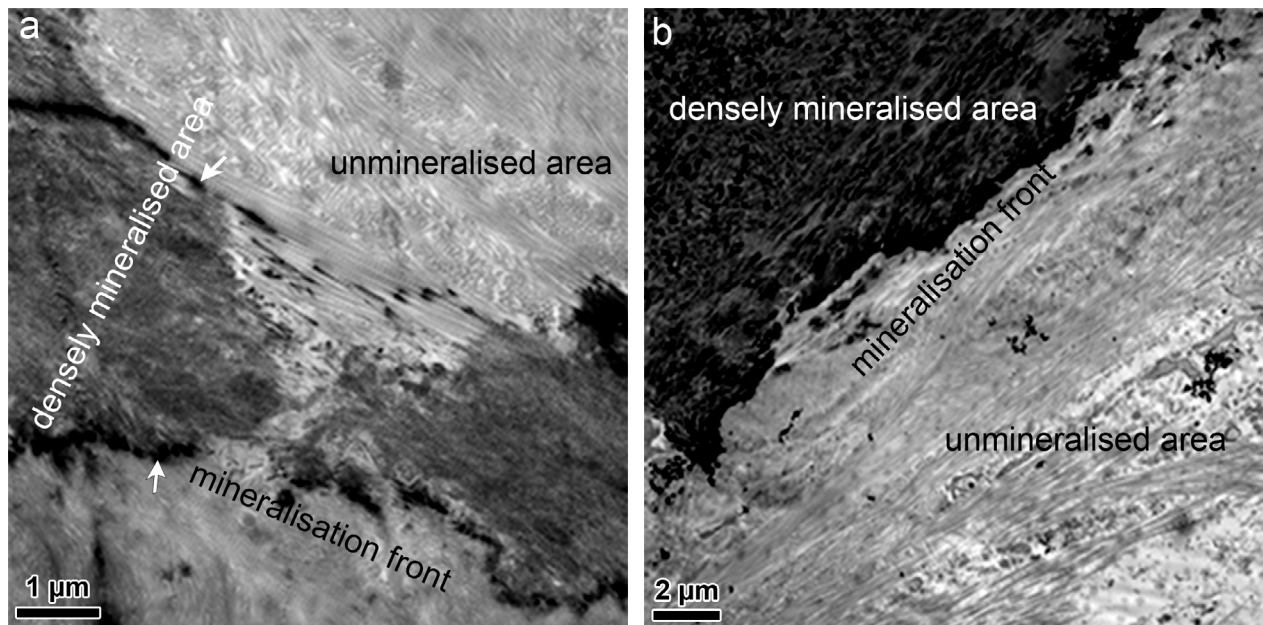


Fig. 11. Ultrastructure of organic matrix and bone mineral material. (a,b) Sample electron micrographs showed the unmineralised organic matrix consisting mostly of collagen fibrils closely packed and parallel arranged. The densely mineralised area revealed a homogenous distribution of the bone mineral substance that localised within and on the collagen fibrils (arrows). At the active mineralisation front, the organic matrix appeared less dense.

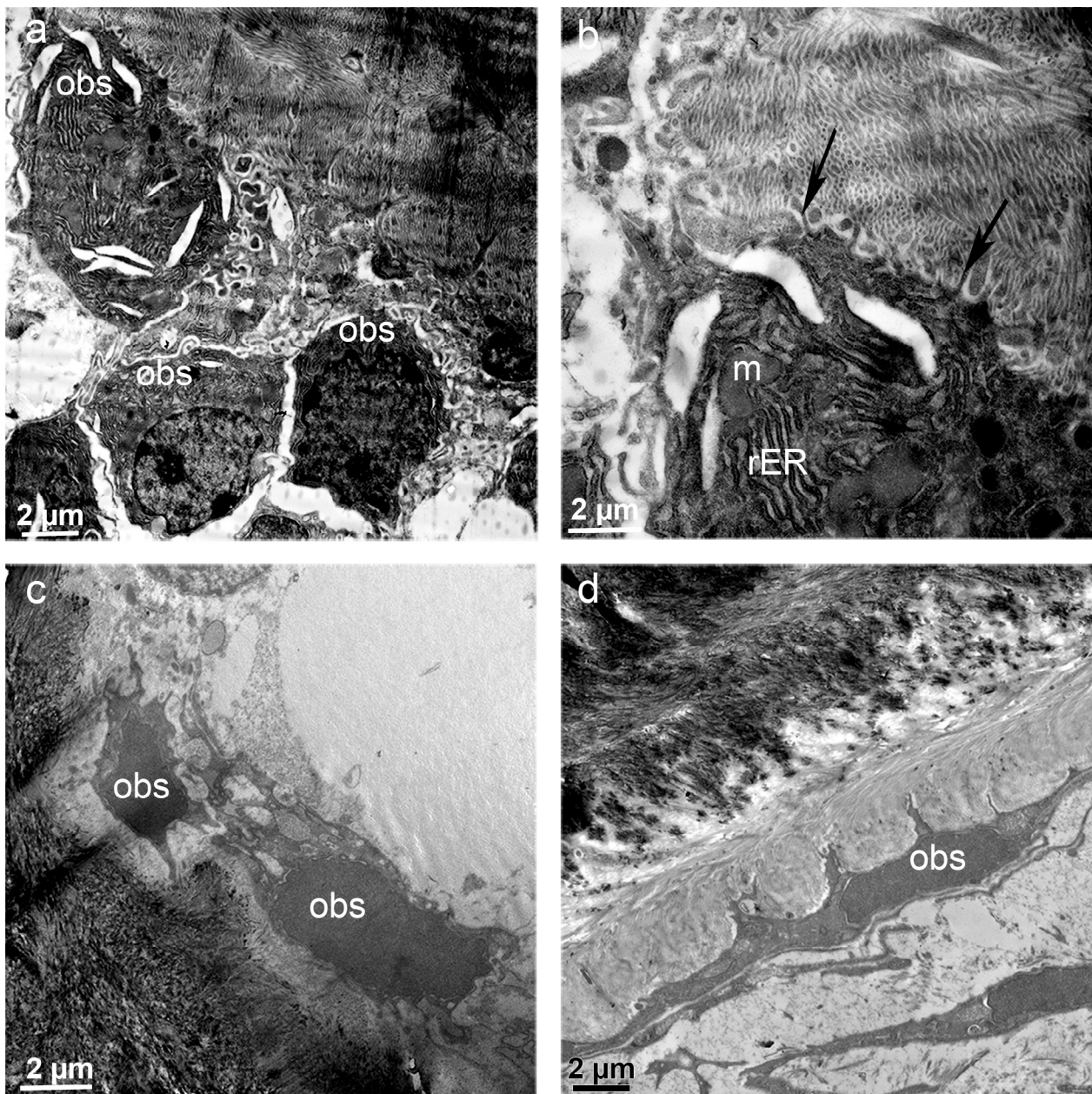


Fig. 12. Osteoblast ultrastructure. (a) Active osteoblasts (obs) in cuboidal shape containing a large nucleus located perpendicular to the bone surface. (b) A close-up image of an obs revealed several electron-dense rough endoplasmic reticulum areas (rER) and mitochondria (m). Osteoblasts were attached to the bone surface by short electron-dense filopodia (arrows). Less active osteoblasts with elongated cytoplasmic extensions that appeared (c) less cuboidal and (d) flattened were evident. The less active osteoblasts occupied the less dense osteoid layer separating them from the more electron dense mineralised bone surface.

the newly formed bone in the fractured area and the native bone outside the fracture area. The line scan, giving the summed signal intensity along the x-axis, revealed higher calcium and collagen signal intensity at the dense cortical bone region in comparison to the trabecular bone region. However, within the fractured gap, the line scans complemented the mappings and demonstrated the presence of calcium and collagen in the fractured area.

Ultrastructural analysis

To further characterise the composition of the organic and inorganic matrix as well as the unique structural

features of osteoblasts, osteoclasts and osteocytes within the new trabeculae, the ultrastructural analysis was carried out by TEM.

Ultrastructure of organic matrix and bone mineral material

The unmineralised organic matrix revealed smooth bundles of collagenous fibres (Fig. 11a,b). The fibrils had a thickness of about 50 nm and were tightly packed together in a parallel orientation, with their architecture resembling that of type I collagen. The organic matrix was homogeneously mineralised by densely distributed bone mineral particle of a few

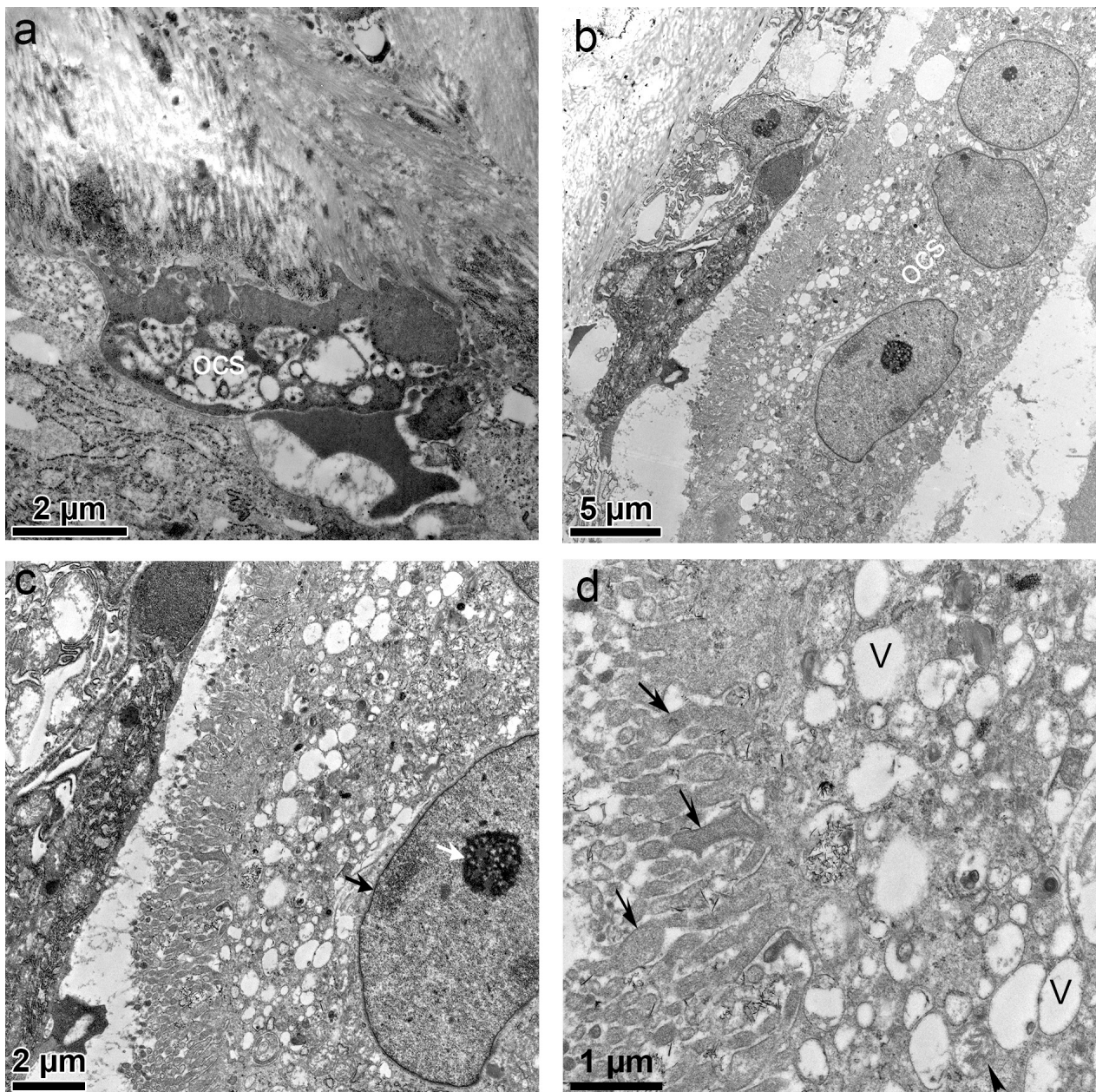


Fig. 13. Osteoclast ultrastructure. Osteoclasts (ocs) actively involved in bone resorption were attached (a) directly to the bone surface and (b) some located near the bone surface. Their large nuclei were positioned away from the resorption area. (c) A higher magnification of b revealed several cytoplasmic components surrounding the nucleus. The nucleus (black arrow) also revealed its highly electron-dense nucleolus, located at the centre (white arrow). (d) A close-up image of the ruffled border showed deep invagination of the cell membrane into the resorption area (arrows). Small and large sized vacuoles (labelled V) and mitochondria (arrow head) localised very close to the ruffled border.

micrometres thickness. Bone mineral deposition was both parallel and perpendicular to the direction of the collagen fibrils. Collagen fibril aggregation increased as more mineral particles were deposited within and on the fibrillar space. The partly mineralised area could be seen at the mineralisation front.

Ultrastructure of osteoblasts

Osteoblasts with different shapes, sizes and arrangements were evident in the new trabeculae. Osteoblasts were actively involved in the secretion of the new bone matrix along the mineralised bone

surface. Active osteoblasts were mostly cuboidal shaped and arranged perpendicularly to the bone surface (Fig. 12a). Their nucleus was positioned opposite to the bone surface. A closer look into one of the osteoblasts revealed numerous rough endoplasmic reticulum areas and mitochondria within the cytoplasm (Fig. 12b). Furthermore, less active osteoblasts that were less rounded (Fig. 12c) and, in some cases, almost flattened along the bone surface (Fig. 12d) were seen located at the osteoid layer, which separated them from the mineralised bone area. Unlike the active osteoblasts, they

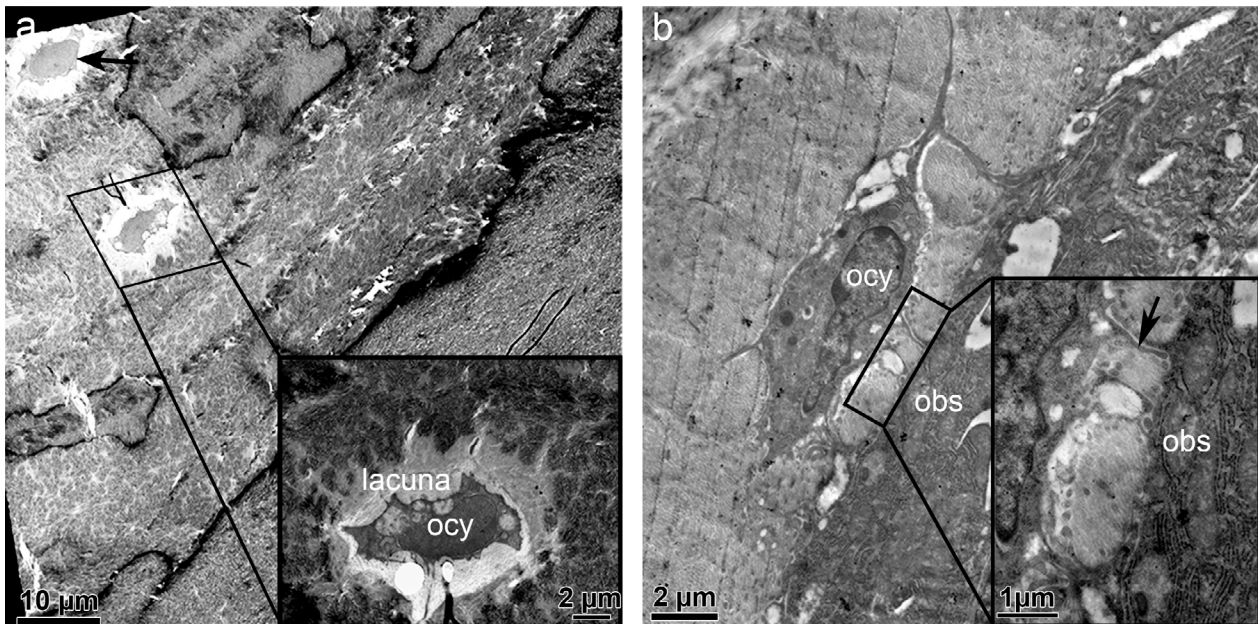


Fig. 14. Osteocyte ultrastructure. (a) Micrograph of the matured star-shaped osteocytes (arrow) embedded within a fully mineralised bone matrix. A close-up image of an osteocyte (see the insert) revealed its flattened periosteocytic lacuna and the prominent nucleus. (b) Micrograph of a young osteocyte localised in the osteoid area and connected through cytoplasmic projections to an adjacent osteoblast. A close-up image of the connecting area, as shown in the insert, revealed long filopodia (arrow) adjoining the osteocyte to the adjacent osteoblast.

appeared less developed and had several elongated cytoplasmic components.

Ultrastructure of osteoclasts

Large multinucleated osteoclasts actively involved in the resorption process were localised at the trabecular bone surface (Fig. 13a) and in the vicinity of bone (Fig. 13b). Their nuclei, surrounded by Golgi apparatus components, were distributed in the cytoplasm and positioned away from the resorption area. Osteoclasts revealed typical prominent ruffled borders, known as active resorption sites, that directly connected them to the bone surface. Numerous large vacuoles, as well as mitochondria, were located very close to the ruffled border (Fig. 13c). A closer look into the ruffled border (Fig. 13d) revealed deep invaginations of the cell membrane in the area of the tissue to be resorbed.

Ultrastructure of osteocytes

Mature star-shaped osteocytes localised individually in flattened periosteocytic lacunae and embedded inside the fully mineralised bone matrix were evident in the new trabeculae (Fig. 14a). Furthermore, osteocytes surrounded by osteoid or partially mineralised bone matrix, referred to as osteoid-osteocytes or young osteocytes, were seen connected by their cytoplasmic extensions to osteoblasts at the bone surface (Fig. 14b). A close-up image of a young osteocyte revealed long filopodia that linked it to the adjacent osteoblast on the bone surface. In comparison to osteoblasts, their nuclei appeared more prominent and their cytoplasm seemed less abundant.

Gene expression analysis

Gene expression of prominent bone formation and resorption markers in the fractured area was investigated by quantitative PCR. Although most of the tested genes appeared to be more expressed in the operated femora, the expressed quantities were not statistically different from those of the unoperated right femora (Fig. 15). The bone turnover markers, namely *COL1A1* – a major extracellular matrix collagenous protein – *BGLAP* and *ALP* – major osteoblast markers known to support bone matrix mineralisation – were increased, whereas *OPG* and *BMP2* were reduced. Furthermore, *COL2A1*, a marker of tissue cartilage, was expressed in negligible quantity in both the operated and unoperated femora (Fig. 15a-f). The reduced expression of *OPG* correlated positively with that of its agonist *RANKL*, which was similarly expressed, resulting in a similar *RANKL/OPG* ratio between operated and unoperated femora (Fig. 15f-h). *CTSK*, a major bone resorption marker, was expressed more in the operated femora relative to the unoperated ones (Fig. 15i).

Discussion

The present study was intended to establish and characterise a clinically relevant metaphyseal fracture model in the distal femur of adult sheep. The three main parameters identified from clinical practice for such a model to be clinically relevant include: i) full discontinuity of the metaphyseal area, ii) comparable internal fixation method and iii)

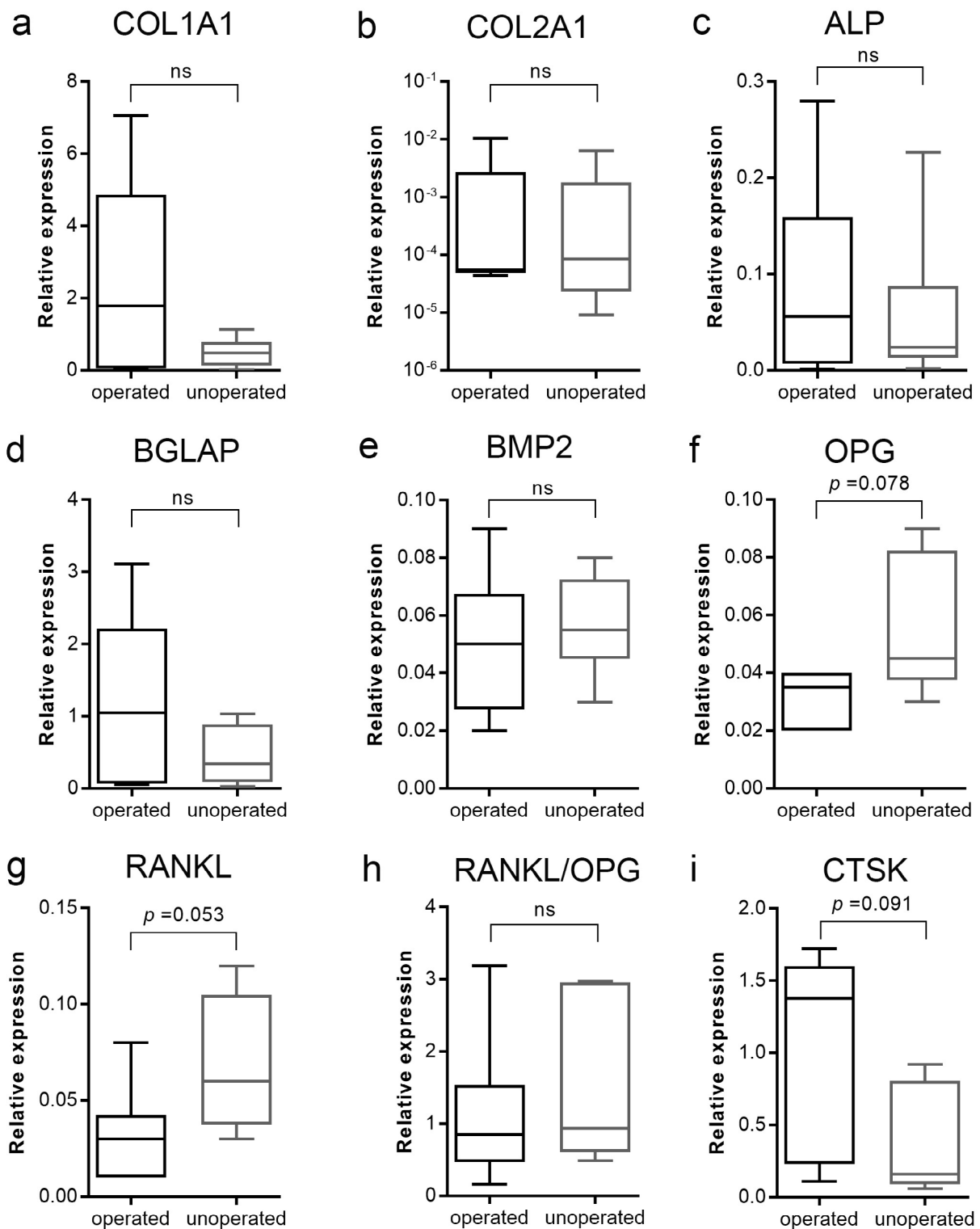


Fig. 15. Relative gene expression analysis using quantitative PCR. Relative expression of major bone formation markers, (a) *Col1A1*, (b) *Col2A1*, (c) *ALP*, (d) *BGLAP*, (e) *BMP2* and (f) *OPG*, and bone resorption markers, (g) *RANKL* and (i) *CTSK*, in the operated left and unoperated right femora. (h) *RANKL/OPG* was similar in both operated and unoperated contralateral femora.

post-operative full-weight bearing of the operated hind limb (Cheung *et al.*, 2016; Wong *et al.*, 2018). The establishment of the fracture gap at the distal metaphyseal region of the femur is of clinical relevance due to the high prevalence of fractures at this bone area (Mosekilde *et al.*, 2000; Riggs and Melton, 1986). To generate full discontinuity at the metaphysis, a wedge-shaped fracture with a medial gap of approximately 0.1 mm and a width of 10 mm at the lateral end of the femoral cortex was chosen. As previously shown in a rat model, the wedge-shape conferred better stability at the medial cortex (Alt *et al.*, 2013). It also eliminates the possible need for an additional fixation at the medial side that would have been necessary in case of a uniformly sized osteotomy. The full discontinuity allows comparison to frequently observed comminution defect zones in metaphyseal fractures in patients. The fracture gap was stabilised internally using a customised titanium locking-plate construct, which is also comparable to the fixation method used in patients with this type of fracture. A major benefit of this fixation technique is the allowance of full-weight bearing without any restriction for the animal. Since the selection of an appropriate time point is essential for achieving a successful bone regeneration, a 12-week healing time was decided upon based on the suggested estimated time of 10-14 weeks for the union of long bone defects in sheep (Mills and Simpson, 2012). Also, previous studies have reported the successful healing outcome at 12 weeks in both human and animal models (Christou *et al.*, 2014; Den Boer *et al.*, 1999; Henderson *et al.*, 2010).

All animals survived the surgical procedure and returned to their normal activity as well as full load bearing around day 3 post-surgery. Also, no form of plate breakage or secondary fracture was seen in the animals throughout the 12-week observation period. Therefore, all three identified parameters could be translated into the presented large animal model. Both the qualitative μ CT and histological evaluation of the bone samples from the medial to the lateral end of the fractured gap showed prominent bony bridging from the medial cortex up to two-thirds of the defect. The lack of external callus formation at the lateral end of the cortex suggested good biomechanical stability achieved by the rigid internal fixation. This observation in the fractured metaphysis is similar to those of Claes *et al.* (1997) who linked periosteal callus formation in the metatarsus diaphysis to the size of interfragmentary movement and strain. They showed that higher interfragmentary movement, even though in the smaller gap, can have a negative impact on the overall diaphyseal fracture healing and the resulting instability most often leads to external callus formation. A similar finding by Henderson *et al.* (2010) showed decreased periosteal callus formation in patients with distal femoral fracture stabilised with a stable locking plate. However, the thin layer of periosteal callus found at the end of the medial cortex, where the defect was only 0.1 mm wide, could

be likely due to minor periodic movements in this region since the major stability was provided at the lateral side of the femur by the locking plate. Such minor periodic movements are beneficial for optimal healing of trabecular bone both in humans and other animals (Claes *et al.*, 2011; Lutz *et al.*, 2015; Vicenti *et al.*, 2014).

The new trabecular bone that bridged the fracture gap formed through direct membranous transformation into bone at the marrow cavity without any observable callus. The absence of cartilaginous tissue within the new trabeculae, as evidenced by the lack of chondrocytes and the negligible quantity of COL2A1, supported the notion of a direct bone transformation without an endochondral healing phase requiring cartilage formation. Cartilaginous tissue formation is linked to instability in both cortical and trabecular bone healing. Thus, the direct transformation into new bone without any cartilage stage could also be attributed to the good biomechanical stability provided by the locking plate. These results supported previous observations that metaphyseal bone healing occurs through a direct intramembranous bone formation under stable biomechanical conditions (Claes *et al.*, 2009; Sandberg and Aspenberg, 2016; Uthoff and Rahn, 1981). Furthermore, the presence of the Haversian system, consisting of tightly packed osteons of concentric lamellae at the newly bridged cortical bone area, is typical for a mature sheep compact bone and, also, similar to that of humans (Kalu, 1999; Martiniaková *et al.*, 2007).

The high healing scores of the μ CT images were good predictors of the healing outcome and correlated with the quantitative μ CT results. The increased bone mass, also evident by the high percentage BV fraction, was comparable to the unoperated contralateral side. The improved quality of the newly formed trabeculae microarchitecture was evident in the derived key morphometric parameters. The significantly thicker trabecular bone and separation of the operated left femur also indicate dense trabeculae with abundant marrow-filled cavities. This suggested that bone healing in the fractured femur was still under remodelling, unlike in the contralateral femur where the aged trabeculae were not in remodelling, hence the thinner trabecular bone (Burr, 2002; Parfitt, 2002). The negative SMI values of the operated femur also suggested dense trabeculae with plate-like structure while the positive SMI value of the unoperated side suggested thinner trabeculae with a more or less rod-like shape (Hildebrand *et al.*, 1999; Hildebrand and Rügsegger, 1997).

The newly formed bone that bridged the fractured gap also attained major matrix mineralisation as seen from the two-fold increase in the mineralised bone area when compared to the osteoid area. ToF-SIMS analysis is an excellent method to identify mineralised tissue (Ray *et al.*, 2018; Thormann *et al.*, 2013). The high calcium signal shows a high level of mineralisation of the newly formed bone matrix. Under-mineralisation

with increased heterogeneity of calcium in the bone matrix is reported in patients with fragility fractures in the metaphyseal area (Fratzl-Zelman *et al.*, 2011). The increased mineralisation correlated positively with the high stiffness measured at both the newly formed cortical and trabecular bone areas of the operated femur, which was quite comparable to the unoperated femur. The higher stiffness recorded at the bridged cortical bone area was in line with previous reports and could be attributed to its unique structural features (Clarke, 2008; Oftadeh *et al.*, 2015; Zysset *et al.*, 1999). Furthermore, the similar distribution pattern observed in the collagen component of the fractured area implied abundant organic matrix. This observation, in agreement with several others, indicated that the quality of both organic and inorganic bone components played a major role in determining the ultimate bone mechanical strength (Wang *et al.*, 2002; Zioupos *et al.*, 1999).

The positive healing outcome was also reflected in the well-established osteocyte-lacuna canaliculi network, which showed proper formation and maturation of the newly formed bone. It also reflected an active involvement of the osteocytes in the regulation of local strains that might have occurred during mechanical loading episodes, thus, suggesting their role in mechanosensing (Aarden *et al.*, 1994; Hemmatian *et al.*, 2017; Klein-Nulend *et al.*, 2013). In small animal models of osteoporosis, osteocyte death is associated with a reduction in bone formation and mechanical strength (Ma *et al.*, 2008; O'Brien *et al.*, 2004). Similarly, bone loss, as reported in ovine and human models of osteoporosis, is caused by low osteocyte density along with an increasing number of empty lacunae (Mullender *et al.*, 2005; Zarrinkalam *et al.*, 2012). Given that the number of osteocytes and their appropriate response to mechanical stimuli is vital to the maintenance of superior bone quality, it is suggested that the increased density of osteocytes lacunae positively influenced the recruitment of active osteoblasts, osteoclasts as well as other relevant growth factors necessary for remodelling.

Changes in osteocyte-lacuna morphology and arrangement are recently proposed to influence the way bone responds to the applied mechanical signal during ageing and/or disease (Hemmatian *et al.*, 2017). A previous study by Carter *et al.* (2013) showed that osteocyte lacunae of the human femora become smaller and spherically shaped with ageing. Ubaidus *et al.* (2009) reported uniformity in the arrangement of the osteocyte-lacuna canaliculi system in healthy bones. In line with the present study observation, they reported that osteocytes align parallel longitudinally to the bone surface and the canaliculi network extends perpendicularly. Therefore, the dominance of spherically shaped osteocyte lacunae along with regular canaliculi system in the newly formed trabeculae of the operated as well as the unoperated femora indicated that the morphological arrangement

of the osteocytes positively influenced their overall function.

High expression of major osteoblasts markers, namely *ALP*, *BGLAP* and *COL1A1*, indicated new bone formation. Increased expression of *ALP* and *BGLAP* could be related to the richly mineralised matrix, which suggested a possible role in mineralisation (Whyte, 1994). *BMP2* is a bone-matrix-derived protein more expressed during the early healing phase and, subsequently, downregulated at the later phase (Cho *et al.*, 2002; Yang *et al.*, 2014; Yu *et al.*, 2010). Hence, its low expression after 12 weeks could be linked to an advanced healing stage. Besides, the stimulation of transforming growth factors, in particular BMPs, is linked to *OPG* production (Schoppet *et al.*, 2002; Udagawa *et al.*, 2000). Thus, the low expression of *BMP2* could be coupled with the decreased amount of *OPG*. Conversely, osteoclastic bone resorption was evident in the expression of *RANKL* and *CTSK* in the operated femora. *CTSK* is a key catabolic enzyme needed for the digestion of the collagenous matrix during bone resorption (Delaissé *et al.*, 2003; Troen, 2006). Hence, its high level was suggestive of an active remodelling phase. Regardless of the high *CTSK* levels, the low level of *RANKL/OPG* indicated that resorption was well coupled with new bone formation, as evident by the increased bone mass. Thus, the high expression of *CTSK* could be related to the study time point. This could imply that high levels of *CTSK* are necessary even at the advanced healing stage since remodelling is still in progress. Since osteoclast-mediated bone resorption is strongly regulated by *RANKL/OPG* (Boyle *et al.*, 2003; Udagawa *et al.*, 2000), their controlled expression by osteoblasts is vital to achieving a balanced remodelling in normal bones.

To further characterise the quality and structural features of the newly formed trabeculae, the ultrastructure of collagen-mineral composite, osteoblasts, osteoclasts and osteocytes was determined by TEM. The typical parallel alignment of the rich collagen fibrils within the organic matrix resembled that of a normal human lamellar bone (Reid, 1986). Major mineralisation of the organic matrix seen in the dense and uniformly distributed bone mineral substance also implied new bone maturation. The mechanical competence of the organic matrix was reinforced by the dense minerals that localised within and on the collagen fibrils (Bonucci, 1984; Lees and Probst, 1988). The less electron dense area observed very near the mineralisation front indicated an ongoing mineralisation. Thus, the unique composition and structural arrangement of the collagen fibrils and the bone mineral substance at the osteoid and mineralised bone areas, respectively, indicated that they both contributed to the final bone quality (Fratzl *et al.*, 2004; Landis, 1995).

The large multinucleated osteoclasts with typical ruffled borders, attached to the surface of the newly formed trabeculae, showed their active and normal

involvement in the remodelling process (Boivin *et al.*, 1990; Domon and Wakita, 1986). The abundant vacuoles situated very close to the ruffled border are necessary for digestion and transportation of cellular debris produced during bone resorption (Marks and Popoff, 1988). Alterations in structure and function of osteoclasts lead to several bone pathologies (Marks, 1984).

The unique morphology and size of osteoblasts revealed their level of activity. Shape, size and arrangement of osteoblasts reflect their activity level (Ries *et al.*, 1985; Zallone, 1977). The plump cuboidal-shaped osteoblasts characterised by a larger surface area and enriched cytoplasmic components, particularly the abundant rough endoplasmic reticulum and mitochondria, indicated their active involvement in the secretion of new bone matrix, whereas the flattened osteoblasts, characterised by several elongated cytoplasmic extensions with a poorly developed cytoplasm, possibly suggested a reduction in activity.

The ultrastructure of the osteocytes differed depending on the level of bone mineralisation. The matured star-shaped osteocytes localised individually in periosteocytic lacunae and were embedded within the fully mineralised bone area. The osteocytes embedded in the osteoid and partially mineralised bone regions connected through their cytoplasmic extensions to adjacent osteoblasts at the bone surface. Those located in the osteoid area are termed osteoid osteocytes, whereas those located in the partially mineralised area are called young osteocytes (Aarden *et al.*, 1994; Palumbo, 1986). Generally, the structure of the osteoid or young osteocytes seemed more developed than the matured osteocytes, indicating that the former probably contributed to bone maturation. Also, by connecting directly to adjacent osteoblasts, young osteocytes could play major roles in inter-cellular communication as well as molecular transport (Sasaki *et al.*, 2012).

Two major limitations of the study were the small sample size and the use of a single observation time point. Although a larger sample size could have improved the outcome of the statistical analysis, this was not possible due to the European welfare act on the use of laboratory animals that encourages the use of a reduced number of animals for experimental purposes. Secondly, additional time points, such as an earlier study time, would have enabled the understanding of the molecular and cellular events occurring during the early phase of bone healing. For example, studying the early phase of bone healing could have provided new insights in to the impact of the initial mechanical condition at the fracture area during the early remodelling phase. However, an additional time point was not possible due to the small sample size.

In conclusion, the study established and characterised a clinically relevant metaphyseal fracture model for metaphyseal bone healing in the distal femur of skeletally mature sheep. In contrast

to the commonly used partial osteotomy model, this novel metaphyseal fracture model was the first large animal model to employ full osteotomy at the metaphysis and use a clinically relevant internal fixation technique to stabilise the fracture area. The customised anatomical locking plate conferred enough mechanical stability to the fractured area, allowing immediate post-operative full-weight bearing. The metaphyseal bone healed through a direct intramembranous bone formation, which was typical and unique to the trabecular bone without visible callus and cartilaginous tissue formation. Therefore, the presented large animal model is highly beneficial for conducting further studies on metaphyseal bone healing, such as the development of treatment options for the enhancement of metaphyseal bone defects.

Acknowledgements

The authors wish to acknowledge the financial support of the German Research Council (DFG) under the project SFB/Transregio 79, sub-project T2. They would also like to express gratitude to Irina Bogun, Ida Oberst, Ivonne Bergen and Gunhild Martels at the Justus-Liebig University of Giessen for their excellent technical assistance.

The authors declare no conflicts of interest.

References

- Aarden EM, Burger EH, Nijweide PJ (1994) Function of osteocytes in bone. *J Cell Biochem* **55**: 287-299.
- Aaron JE, Skerry TM (1994) Intramembranous trabecular generation in normal bone. *Bone Miner* **25**: 211-230.
- Alt V, Thormann U, Ray S, Zahner D, Dürselen L, Lips K, El Khassawna T, Heiss C, Riedrich A, Schlewitz G, Ignatius A, Kampschulte M, Von Dewitz H, Heinemann S, Schnettler R, Langheinrich A (2013) A new metaphyseal bone defect model in osteoporotic rats to study biomaterials for the enhancement of bone healing in osteoporotic fractures. *Acta Biomater* **9**: 7035-7042.
- Beil FT, Barvencik F, Gebauer M, Seitz S, Rueger JM, Ignatius A, Pogoda P, Schinke T, Amling M (2010) Effects of estrogen on fracture healing in mice. *J Trauma Inj Infect Crit Care* **69**: 1259-1265.
- Bindl R, Oheim R, Pogoda P, Beil FT, Gruchenberg K, Reitmaier S, Wehner T, Calcia E, Radermacher P, Claes L, Amling M, Ignatius A (2013) Metaphyseal fracture healing in a sheep model of low turnover osteoporosis induced by hypothalamic-pituitary disconnection (HPD). *J Orthop Res* **31**: 1851-1857.
- Boivin G, Anthoine-Terrier C, Obrant KJ (1990) Transmission electron microscopy of bone tissue. A review. *Acta Orthop Scand* **61**: 170-180.

- Bonucci E (1984) The structural basis of calcification. In: *Ultrastructure of the connective tissue matrix*. Ed: Ruggeri A, Motta PM. Springer, Boston, MA, USA. pp: 165-191.
- Bouxsein ML, Boyd SK, Christiansen BA, Guldberg RE, Jepsen KJ, Müller R (2010) Guidelines for assessment of bone microstructure in rodents using micro-computed tomography. *J Bone Miner Res* **25**: 1468-1486.
- Boyle WJ, Simonet WS, Lacey DL (2003) Osteoclast differentiation and activation. *Nature* **423**: 337-42.
- Burr DB (2002) Targeted and nontargeted remodeling. *Bone* **30**: 2-4.
- Carter Y, Thomas CDL, Clement JG, Cooper DML (2013) Femoral osteocyte lacunar density, volume and morphology in women across the lifespan. *J Struct Biol* **183**: 519-526.
- Cheung WH, Micalau T, Chow SKH, Yang FF, Alt V (2016) Fracture healing in osteoporotic bone. *Injury* **47**: S21-S26.
- Cho TJ, Gerstenfeld LC, Einhorn TA (2002) Differential temporal expression of members of the transforming growth factor β superfamily during murine fracture healing. *J Bone Miner Res* **17**: 513-520.
- Christou C, Oliver RA, Pelletier MH, Walsh WR (2014) Ovine model for critical-size tibial segmental defects. *Comp Med* **64**: 377-385.
- Claes L, Augat P, Suger G, Wilke HJ (1997) Influence of size and stability of the osteotomy gap on the success of fracture healing. *J Orthop Res* **15**: 577-584.
- Claes LE, Wilke H-J, Augat P, Rübenacker S, Margevicius KJ (1995) Effect of dynamization on gap healing of diaphyseal fractures under external fixation. *Clin Biomech (Bristol, Avon)* **10**: 227-234.
- Claes L, Reusch M, Göckelmann M, Ohnmacht M, Wehner T, Amling M, Beil FT, Ignatius A (2011) Metaphyseal fracture healing follows similar biomechanical rules as diaphyseal healing. *J Orthop Res* **29**: 425-432.
- Claes L, Veerer A, Göckelmann M, Simon U, Ignatius A (2009) A novel model to study metaphyseal bone healing under defined biomechanical conditions. *Arch Orthop Trauma Surg* **129**: 923-928.
- Clarke B (2008) Normal bone anatomy and physiology *Clin J Am Soc Nephrol* **3** Suppl 3: S131-139.
- Delaissé J-M, Andersen TL, Engsig MT, Henriksen K, Troen T, Blavier L (2003) Matrix metalloproteinases (MMP) and cathepsin K contribute differently to osteoclastic activities. *Microsc Res Tech* **61**: 504-513.
- Den Boer FC, Patka P, Bakker FC, Wipperfmann BW, Van Lingen A, Vink GQM, Boshuizen K, Haarman HJTM (1999) New segmental long bone defect model in sheep: quantitative analysis of healing with dual energy x-ray absorptiometry. *J Orthop Res* **17**: 654-660.
- Domon T, Wakita M (1986) Electron microscope study of osteoclasts with special reference to the three-dimensional structure of the ruffled border. *Arch Histol Jpn* **49**: 593-602.
- Fan W, Crawford R, Xiao Y (2008) Structural and cellular differences between metaphyseal and diaphyseal periosteum in different aged rats. *Bone* **42**: 81-89.
- Fletcher JS, Vickerman JC (2010) A new SIMS paradigm for 2D and 3D molecular imaging of bio-systems. *Anal Bioanal Chem* **396**: 85-104.
- Fratzl-Zelman N, Roschger P, Misof BM, Nawrot-Wawrzyniak K, Pötter-Lang S, Muschitz C, Resch H, Klaushofer K, Zwettler E (2011) Fragility fractures in men with idiopathic osteoporosis are associated with undermineralization of the bone matrix without evidence of increased bone turnover. *Calcif Tissue Int* **88**: 378-387.
- Fratzl P, Gupta HS, Paschalis EP, Roschger P (2004) Structure and mechanical quality of the collagen-mineral nano-composite in bone. *J Mater Chem* **14**: 2115-2123.
- Hemmatian H, Bakker AD, Klein-Nulend J, van Lenthe GH (2017) Aging, osteocytes, and mechanotransduction. *Curr Osteoporos Rep* **15**: 401-411.
- Henderson CE, Lujan T, Bottlang M, Fitzpatrick DC, Madey SM, Marsh JL (2010) Stabilization of distal femur fractures with intramedullary nails and locking plates: differences in callus formation. *Iowa Orthop J* **30**: 61-68.
- Henss A, Rohnke M, ElKhassawna T, Govindarajan P, Schlewitz G, Heiss C, Janek J (2013) Applicability of ToF-SIMS for monitoring compositional changes in bone in a long-term animal model. *J R Soc Interface* **10**: 20130332-20130332.
- Hildebrand T, Laib A, Müller R, Dequeker J, Rüeegsegger P (1999) Direct three-dimensional morphometric analysis of human cancellous bone: microstructural data from spine, femur, iliac crest, and calcaneus. *J Bone Miner Res* **14**: 1167-1174.
- Hildebrand T, Rüeegsegger P (1997) Quantification of bone microarchitecture with the structure model index. *Comput Methods Biomech Biomed Engin* **1**: 15-23.
- Kalu DN (1999) Animal models of the aging skeleton. In: *The Aging Skeleton*. Ed: Glowacki J, Rosen CJ, Bilezikian JP. 1st ed Academic Press, Elsevier. pp: 37-50.
- Klein-Nulend J, Bakker AD, Bacabac RG, Vatsa A, Weinbaum S (2013) Mechanosensation and transduction in osteocytes. *Bone* **54**: 182-190.
- Komori T (2015) Animal models for osteoporosis. *Eur J Pharmacol* **759**: 287-294.
- Landis WJ (1995) The strength of a calcified tissue depends in part on the molecular structure and organization of its constituent mineral crystals in their organic matrix. *Bone* **16**: 533-544.
- Lees S, Probst K (1988) The locus of mineral crystallites in bone. *Connect Tissue Res* **18**: 41-54.
- Lill CA, Hessel J, Schlegel U, Eckhardt C, Goldhahn J, Schneider E (2003) Biomechanical evaluation of healing in a non-critical defect in a large animal model of osteoporosis. *J Orthop Res* **21**: 836-842.

- Livak KJ, Schmittgen TD (2001) Analysis of relative gene expression data using real-time quantitative PCR and the 2(-Delta Delta C(T)). *Method Methods* **25**: 402-408.
- Lutz M, Steck R, Sitte I, Rieger M, Schuetz M, Klestil T (2015) The metaphyseal bone defect in distal radius fractures and its implication on trabecular remodeling—a histomorphometric study (case series). *J Orthop Surg Res* **10**: 1-7.
- Ma Y-L, Dai R-C, Sheng Z-F, Jin Y, Zhang Y-H, Fang L-N, Fan H-J, Liao E-Y (2008) Quantitative associations between osteocyte density and biomechanics, microcrack and microstructure in OVX rats vertebral trabeculae. *J Biomech* **41**: 1324-1332.
- Malhotra A, Pelletier MH, Yu Y, Christou C, Walsh WR (2014) A sheep model for cancellous bone healing. *Front Surg* **1**: 37. DOI: 10.3389/fsurg.2014.00037.
- Marks SC (1984) Congenital osteopetrotic mutations as probes of the origin, structure, and function of osteoclasts *Clin Orthop Relat Res*: 239-263.
- Marks SC, Popoff SN (1988) Bone cell biology: the regulation of development, structure, and function in the skeleton. *Am J Anat* **183**: 1-44.
- Martini L, Fini M, Giavaresi G, Giardino R (2001) Sheep model in orthopedic research: a literature review. *Comp Med* **51**: 292-299.
- Martiniaková M, Grosskopf B, Omelka R, Vondráková M, Bauerová M (2007) Histological analysis of ovine compact bone tissue. *J Vet Med Sci* **69**: 409-411.
- Meyer RA, Tsahakis PJ, Martin DF, Banks DM, Harrow ME, Kiebzak GM (2001) Age and ovariectomy impair both the normalization of mechanical properties and the accretion of mineral by the fracture callus in rats. *J Orthop Res* **19**: 428-435.
- Mills LA, Simpson AHRW (2012) *In vivo* models of bone repair. *J Bone Joint Surg Br* **94**: 865-874.
- Morgan EF, Mason ZD, Chien KB, Pfeiffer AJ, Barnes GL, Einhorn TA, Gerstenfeld LC (2009) Micro-computed tomography assessment of fracture healing: relationships among callus structure, composition, and mechanical function. *Bone* **44**: 335-344.
- Mosekilde L, Ebbesen EN, Tornvig L, Thomsen JS (2000) Trabecular bone structure and strength - remodelling and repair. *J Musculoskelet Neuronal Interact* **1**: 25-30.
- Mullender MG, Tan SD, Vico L, Alexandre C, Klein-Nulend J (2005) Differences in osteocyte density and bone histomorphometry between men and women and between healthy and osteoporotic subjects. *Calcif Tissue Int* **77**: 291-296.
- Nyman JS, Munoz S, Jadhav S, Mansour A, Yoshii T, Mundy GR, Gutierrez GE (2009) Quantitative measures of femoral fracture repair in rats derived by micro-computed tomography. *J Biomech* **42**: 891-897.
- O'Brien CA, Jia D, Plotkin LI, Bellido T, Powers CC, Stewart SA, Manolagas SC, Weinstein RS (2004) Glucocorticoids act directly on osteoblasts and osteocytes to induce their apoptosis and reduce bone formation and strength. *Endocrinology* **145**: 1835-1841.
- Oftadeh R, Entezari V, Sporri G, Villa-Camacho JC, Krigbaum H, Strawich E, Graham L, Rey C, Chiu H, Muller R, Hashemi HN, Vaziri A, Nazarian A (2015) Hierarchical analysis and multi-scale modelling of rat cortical and trabecular bone. *J R Soc Interface* **12**: 20150070-20150070.
- Palumbo C (1986) A three-dimensional ultrastructural study of osteoid-osteocytes in the tibia of chick embryos. *Cell Tissue Res* **246**: 125-131.
- Parfitt AM (2002) Targeted and nontargeted bone remodeling: relationship to basic multicellular unit origination and progression *Bone* **30**: 5-7.
- Rabie A-BM, Dan Z, Samman N (1996) Ultrastructural identification of cells involved in the healing of intramembranous and endochondral bones. *Int J Oral Maxillofac Surg* **25**: 383-388.
- Ray S, Thormann U, Eichelroth M, Budak M, Biehl C, Rupp M, Sommer U, El Khassawna T, Alagboso FI, Kampschulte M, Rohnke M, Henß A, Peppler K, Linke V, Quadbeck P, Voigt A, Stenger F, Karl D, Schnettler R, Heiss C, Lips KS, Alt V (2018) Strontium and bisphosphonate coated iron foam scaffolds for osteoporotic fracture defect healing *Biomaterials* **157**: 1-16.
- Reid SA (1986) A study of lamellar organisation in juvenile and adult human bone. *Anat Embryol (Berl)* **174**: 329-338.
- Ries WL, Gong JK, Sholley MM (1985) A comparative study of osteoblasts: *in situ versus* isolated specimens *Am J Anat* **172**: 57-73.
- Riggs BL, Melton LJ (1986) Involutional osteoporosis. *N Engl J Med* **314**: 1676-1686.
- Sandberg OH, Aspenberg P (2016) Inter-trabecular bone formation: a specific mechanism for healing of cancellous bone: a narrative review. *Acta Orthop* **87**: 459-465.
- Sasaki M, Hongo H, Hasegawa T, Suzuki R, Zhusheng L, de Freitas PHL, Yamada T, Oda K, Yamamoto T, Li M, Totsuka Y, Amizuka N (2012) Morphological aspects of the biological function of the osteocytic lacunar canalicular system and of osteocyte-derived factors. *Oral Sci Int* **9**: 1-8.
- Schoppet M, Preissner KT, Hofbauer LC (2002) RANK ligand and osteoprotegerin: paracrine regulators of bone metabolism and vascular function. *Arterioscler Thromb Vasc Biol* **22**: 549-553.
- Schueler BW (2013) Time-of-flight mass analysers. In *TOF-SIMS Materials Analysis by Mass Spectrometry*, 2nd Edition. Eds: Vickerman JC, Briggs D, IM Publications LLP, ISBN: 978-1-906715-17-Z pp 247-270
- Simpson AH, Murray IR (2016) Main differences in osteoporotic fracture models: which should I use? *Injury* **47**: S15-S20.
- Thormann U, Ray S, Sommer U, Elkhassawna T, Rehling T, Hundgeburth M, Henß A, Rohnke M, Janek J, Lips KS, Heiss C, Schlewitz G, Szalay G, Schumacher M, Gelinsky M, Schnettler R, Alt

V (2013) Bone formation induced by strontium modified calcium phosphate cement in critical-size metaphyseal fracture defects in ovariectomized rats. *Biomaterials* **34**: 8589-8598.

Troen BR (2006) The regulation of cathepsin K gene expression. *Ann N Y Acad Sci* **1068**: 165-172.

Turner AS (2002) The sheep as a model for osteoporosis in humans. *Vet J* **163**: 232-239.

Turner AS, Alvis M, Myers W, Stevens ML, Lundy MW (1995) Changes in bone mineral density and bone-specific alkaline phosphatase in ovariectomized ewes. *Bone* **17**: 395-402.

Ubaidus S, Li M, Sultana S, De Freitas PHL, Oda K, Maeda T, Takagi R, Amizuka N (2009) FGF23 is mainly synthesized by osteocytes in the regularly distributed osteocytic lacunar canalicular system established after physiological bone remodeling. *J Electron Microscop* (Tokyo) **58**: 381-392.

Udagawa N, Takahashi N, Yasuda H, Mizuno A, Itoh K, Ueno Y, Shinki T, Gillespie MT, Martin TJ, Higashio K, Suda T (2000) Osteoprotegerin produced by osteoblasts is an important regulator in osteoclast development and function. *Endocrinology* **141**: 3478-3484.

Uthoff HK, Rahn BA (1981) Healing patterns of metaphyseal fractures. *Clin Orthop Relat Res*: 295-303.

Vicenti G, Pesce V, Tartaglia N, Abate A, Mori CM, Moretti B (2014) Micromotion in the fracture healing of closed distal metaphyseal tibial fractures: a multicentre prospective study. *Injury* **45**: S27-S35.

Wang X, Shen X, Li X, Agrawal CM (2002) Age-related changes in the collagen network and toughness of bone. *Bone* **31**: 1-7.

Whyte MP (1994) Hypophosphatasia and the role of alkaline phosphatase in skeletal mineralization. *Endocr Rev* **15**: 439-61.

Wong RMY, Choy MH V., Li MCM, Leung K-S, K-H Chow S, Cheung W-H, Cheng JCY (2018) A systematic review of current osteoporotic metaphyseal fracture animal models. *Bone Joint Res* **7**: 6-11.

Yang J, Shi P, Tu M, Wang Y, Liu M, Fan F, Du M (2014) Bone morphogenetic proteins: relationship between molecular structure and their osteogenic activity. *Food Sci Hum Wellness* **3**: 127-135.

Yu YY, Lieu S, Lu C, Miclau T, Marcucio RS, Colnot C (2010) Immunolocalization of BMPs, BMP antagonists, receptors, and effectors during fracture repair. *Bone* **46**: 841-851.

Zallone AZ (1977) Relationships between shape and size of the osteoblasts and the accretion rate of trabecular bone surfaces. *Anat Embryol (Berl)* **152**: 65-72.

Zarrinkalam MR, Beard H, Schultz CG, Moore RJ (2009) Validation of the sheep as a large animal model

for the study of vertebral osteoporosis. *Eur Spine J* **18**: 244-253.

Zarrinkalam MR, Mulaibrahimovic A, Atkins GJ, Moore RJ (2012) Changes in osteocyte density correspond with changes in osteoblast and osteoclast activity in an osteoporotic sheep model. *Osteoporos Int* **23**: 1329-1336.

Zioupou P, Currey JD, Hamer AJ (1999) The role of collagen in the declining mechanical properties of aging human cortical bone. *J Biomed Mater Res* **45**: 108-116.

Zysset PK, Edward Guo X, Edward Hoffler C, Moore KE, Goldstein SA (1999) Elastic modulus and hardness of cortical and trabecular bone lamellae measured by nanoindentation in the human femur. *J Biomech* **32**: 1005-1012.

Discussion with Reviewers

Devakar Epari: Are the properties of an ideal biomaterial to augment metaphyseal bone regeneration different from those to support diaphyseal defects?

Authors: Since the characteristic healing pattern of a metaphyseal fracture differs from that of a diaphyseal fracture due to their different mechanical and biological environment, the properties of an ideal biomaterial to augment bone regeneration in both regions should be different. For example, a resorbable bone regenerative material would be more suitable for the treatment of a metaphyseal fracture, whereas a non-resorbable bone substitute material would be more appropriate for a diaphyseal fracture.

Wing Hoi Cheung: What kind of research do you suggest being most suitable to use this animal model for?

Authors: This animal model will be beneficial to study future treatment options, e.g. using novel composite biomaterials to locally augment the healing of metaphyseal bone fractures.

Wing Hoi Cheung: Do you think week 12 post-surgery can be regarded as complete healing?

Authors: Based on the findings of the study, 12 weeks post-surgery could be considered as an appropriate time to generate complete bone healing under mechanically stable condition in a normal metaphyseal bone fracture since an advanced healing outcome was achieved naturally without any external material.

Editor's note: The Scientific Editor responsible for this paper was Juerg Gasser.